

Search for Spatially Extended *Fermi*-LAT Sources Using Two Years of Flight Data

J. Lande², S. Funk², M. Ackermann (???), ...

ABSTRACT

Spatial extension is an important characteristic for correctly associating LAT sources with their counterparts at other wavelengths and for obtaining an unbiased model of their spectra. We present a new method for quantifying the spatial extension of sources with the Large Area Telescope (LAT), the primary science instrument on the *Fermi Gamma-ray Space Telescope* (*Fermi*). We perform a series of Monte Carlo simulations to validate this tool and calculate the LAT's threshold for detecting the spatial extension of sources. We then test all sources in the second *Fermi*-LAT catalog (2FGL) for extension. We report the detection of nine spatially extended sources in addition to the twelve spatially extended sources reported in 2FGL.

Subject headings: Catalogs; Fermi Gamma-ray Space Telescope; Gamma rays: observations; ISM: supernova remnants; Methods: statistical; pulsar wind nebula

1. Introduction

A number of astrophysical source classes including supernova remnants (SNRs), pulsar wind nebulae (PWNe), molecular clouds, normal galaxies, and galaxy clusters are expected to be spatially resolvable at GeV energies. Dark matter satellites are also hypothesized to be spatially extended. The Large Area Telescope (LAT) on the *Fermi Gamma-ray Space Telescope* (*Fermi*) has detected seven SNRs which are significantly extended at GeV energies: W51C, W30, IC443, W28, W44, RX J1713.7–3946, and the Cygnus Loop (Abdo et al. 2009c; Castro & Slane 2010; Abdo et al. 2010h,e,g, 2011c; Katagiri et al. 2011). In addition, three extended PWNe were detected as being extended: MSH 15–52, Vela X, and

²W. W. Hansen Experimental Physics Laboratory, Kavli Institute for Particle Astrophysics and Cosmology, Department of Physics and SLAC National Accelerator Laboratory, Stanford University, Stanford, CA 94305, USA

⁵³Institut für Astronomie und Astrophysik, Universität Tübingen, D 72076 Tübingen, Germany

HESS J1825–137 (Abdo et al. 2010a,f; Grondin et al. 2011). Two close-by galaxies, the Large and Small Magalenic Clouds, and one radio galaxy, Centarus A, were spatially resolved at GeV energies (Abdo et al. 2010i,b,c). A number of additional sources detected at GeV energies are positionally coincident with sources that exhibit extension at other wavelengths, large enough to be spatially resolvable by the LAT at GeV energies.

The current generation of air Cherenkov detectors have made it apparent that many sources can be spatially resolved at even higher energies. Most prominent was a survey of the Galactic plane using the High Energy Stereoscopic System (H.E.S.S) which reported 14 spatially extended sources with extensions varying from $\sim 0^\circ.1$ to $\sim 0^\circ.25$ (Aharonian et al. 2006). In fact, within our Galaxy only very few sources detected at TeV energies (most notably the γ -ray binaries LS 5039 (Aharonian et al. 2006a), LS I+61–303 (Albert et al. 2006; Acciari et al. 2011) HESS J0632+057 (Aharonian et al. 2007c), and the Crab nebula (Weekes et al. 1989)) have no detectable extension. High-energy γ -rays from these sources are produced by the decay of π^0 s produced by hadronic interactions with interstellar matter and by relativistic electrons due to Inverse Compton (IC) scattering and Bremsstrahlung radiation (Blandford & Eichler 1987). It is likely that the GeV and TeV emission from these sources originates from the same population of high-energy particles and so at least some of these sources should be detected at GeV energies. Studying these TeV sources at GeV energies would help to determine the emission mechanisms producing these high energy photons.

The LAT is a pair conversion telescope that has been surveying the γ -ray sky since 2008 June. The LAT has broad energy coverage (20 MeV to > 300 GeV), wide field of view (~ 2.4 sr), and large effective area (~ 8000 cm² at > 1 GeV). Using one year of all-sky surveying data, the LAT Collaboration published a catalog of 1451 sources significantly detected at GeV energies called 1FGL (Abdo et al. 2010d). Using two years of data, a second catalog called 2FGL reported on 1873 sources (Abdo et al. 2011b). The counterparts of many of these sources can be spatially resolved when observed at other frequencies but detecting the spatial extension of these sources at GeV energies is difficult because the size of the point-spread function (PSF) of the LAT is comparable to the typical size of many of these sources.

The capability to spatially resolve GeV γ -ray sources is important for several reasons. Finding a coherent source extension across different energy bands can help to associate a LAT source to an otherwise confused counterpart. Furthermore, some of the dark matter substructure in our Galaxy is predicted to be spatially extended at GeV energies (Baltz et al. 2008). Characterization of spatial extension could help to identify this substructure. Also, due to the strong energy dependence of the LAT PSF, the spatial and spectral character of

a source do not decouple. An inaccurate spatial model will bias the spectral model of the source and vice versa. Specifically, modeling a spatially extended source as point-like will systematically shift a spectral analysis to softer indices. Furthermore, correctly modeling a source’s extension is important for understanding an entire region of the sky. For example, an incorrect model of the spatially extended LMC introduced significant residuals in the surrounding region (Abdo et al. 2010d, 2011b). Such residuals can bias the significance and measured spectrum of neighboring sources in the densely populated Galactic plane.

Previous analysis of extended LAT sources were performed as dedicated studies of individual sources, so we expect that a systematic scan of all LAT detected sources could uncover additional spatially extended sources. For these reasons, in Section 2 we present a new systematic method for analyzing spatially extended LAT sources. In Section 3 we demonstrate that this method can be used to test the statistical significance of the extension of a LAT sources and in Section 4 we calculate the LAT’s detection threshold to resolve the extension of a source. In Section 5 we describe a search for new spatially extended LAT sources and in Section 6 we reanalyze the twelve previously detected extended sources included in 2FGL. In Section 7 we further demonstrate that our detection method does not misidentify point sources as being extended by testing the extension of active galactic nuclei (AGN) believed to be unresolvable. Finally, in Section 8 we present the detection of the extension of nine spatially extended sources that were reported in 2FGL but not previously spatially resolved.

2. Analysis Methods

Morphological studies of sources using the LAT are challenging because of the strongly energy-dependent PSF that is comparable in size to the extension of many sources expected to be detected at GeV energies. Additional complications arise for sources along the Galactic plane due to systematic uncertainties in the Galactic diffuse emission. The LAT’s PSF is limited at its lowest detectable energies by multiple scattering in the silicon strip tracking section of the detector and is several degrees at 100 MeV. The PSF improves with energy approaching a 68% containment radius of $\sim 0^\circ.2$ at the highest energies (when averaged over the acceptance of the LAT) and is limited by the granularity of the silicon strips in the tracker (Atwood et al. 2009; Abdo et al. 2009f, 2011a).¹ However, since most high energy astrophysical sources have spectra that decrease rapidly with increasing energy, the improved resolution of the higher energy photons is offset by their low statistics. Therefore

¹More information about the performance of the LAT can be found at the *Fermi* Science Support Center (FSSC, <http://fermi.gsfc.nasa.gov>).

sophisticated analysis techniques are required to maximize our sensitivity to these extended sources.

2.1. The pointlike Package

A new analysis tool has been developed to address the unique requirements for studying spatially extended sources with the LAT. The tool performs a maximum likelihood analysis in which the Poisson likelihood to find the observing counts is maximized given a parametrized spatial and spectral model of the source and its surrounding region. The sky is divided into cubes in space and energy using the healpix representation of the sky (Górski et al. 2005) and the likelihood is maximized over all bins in a region. The extension of a source can be modeled by a geometric shape (e.g. a disk or a two-dimensional Gaussian) and the source’s position, extension, and spectrum can be simultaneously fit.

This type of analysis is not feasible using the standard LAT likelihood analysis tool `gtlike`² because it can only fit the spectral parameters of the model unless a more sophisticated iterative procedure is used to also test various source morphologies. We note that `gtlike` has been used in the past in several studies of source extension in the LAT Collaboration (Abdo et al. 2010i,b,e, 2009c). In these studies, a profile based upon a set of `gtlike` maximum likelihood fits at fixed extensions was used to build a profile of the likelihood as a function of extension. This approach is not optimal because the position, extension, and spectrum of the source must be simultaneously fit to find the best fit parameters and to correctly compute the statistical significance of a detection. Furthermore since the `gtlike` likelihood profile approach is computationally intensive, no large-scale Monte Carlo simulations have been run to validate it.

The approach presented here is based on a second maximum likelihood fitting package developed in the LAT Collaboration called `pointlike` (Abdo et al. 2010d; Kerr 2011). The choice to base the spatial extension fitting on `pointlike` rather than `gtlike` was made on considerations of computing time. The `pointlike` algorithm was optimized for speed to handle larger numbers of sources efficiently which is important for our catalog scan and for being able to perform large-scale Monte Carlo simulations to validate the tool. Details on the `pointlike` package can be found in Kerr (2011). We extended the code to allow a simultaneous fit of the source extension together with the position and the spectral parameters.

²`gtlike` is distributed publicly by the FSSC.

2.2. Extension Fitting

In **pointlike**, it is assumed that the spatial and spectral model of an extended source are separable, i.e. that the source model $M(l, b, E) = S(l, b) \times X(E)$ where $S(l, b)$ is the spatial distribution and $X(E)$ is the spectral distribution. To fit an extended source, **pointlike** convolves the extended source shape with the PSF (as a function of energy) and uses the **minuit** library (James & Roos 1975) to maximize the likelihood by simultaneously varying the position and extension of the source. As will be described in Section 3, simultaneously fitting the position and extension is important to correctly calculate the statistical significance of the detection of extension. For each position and extension, the spectral parameters of the sky model are refit. To avoid projection effects, the fitted source position parameters are not the source’s longitude and latitude but instead the source’s displacement in a rotated reference frame.

The significance of the extension of a source can be calculated from the likelihood ratio test of a model with a spatially extended source and a model with a point-like source. The test statistic for this procedure is defined as

$$\text{TS}_{\text{ext}} = 2 \log(\mathcal{L}_{\text{ext}}/\mathcal{L}_{\text{ps}}) \quad (1)$$

where \mathcal{L} is the Poisson likelihood. **pointlike** calculates TS_{ext} by fitting a source first with a spatially extended model and then as a point source. The interpretation of TS_{ext} in terms of a statistical significance is discussed in Section 3.

For extended sources with an assumed radially symmetric shape, we can optimize the calculation by performing one of the integrals analytically. The expected photon distribution can be written as

$$\text{PDF}(\vec{r}) = \int \text{PSF}(|\vec{r} - \vec{r}'|) I_{\text{src}}(\vec{r}') r' dr' d\phi' \quad (2)$$

For the LAT, the PSF can be parameterized by a King function (King 1962):

$$\text{PSF}(r) = \frac{1}{2\pi\sigma^2} \left(1 - \frac{1}{\gamma}\right) \left(1 + \frac{u}{\gamma}\right)^{-\gamma}, \quad (3)$$

where $u = (r/\sigma)^2/2$ and σ and γ are free parameters (Kerr 2011). For radially symmetric extended sources, the angular part of the integral can be evaluated analytically

$$\begin{aligned} \text{PDF}(u) &= \int_0^\infty r' dr' I_{\text{src}}(v) \int_0^{2\pi} d\phi' \text{PSF}(\sqrt{2\sigma^2(u + v - 2\sqrt{uv}\cos(\phi - \phi'))}) \\ &= \int_0^\infty dv I_{\text{src}}(v) \left(\frac{\gamma - 1}{\gamma}\right) \left(\frac{\gamma}{\gamma + u + v}\right)^\gamma \times {}_2F_1\left(\gamma/2, \frac{1 + \gamma}{2}, 1, \frac{4uv}{(\gamma + u + v)^2}\right). \end{aligned} \quad (4)$$

$$(5)$$

where $v = (r'/\sigma)^2/2$ and ${}_2F_1$ is the Gaussian hypergeometric function. This convolution formula reduces the expected photon distribution to a single numerical integral.

There will always be a small numerical discrepancy between the expected photon distribution derived from a true point source and a very small extended source due to numerical error in the convolution. In most situations, this error is insignificant. But in particular for very bright sources, this numerical error has the potential to bias the test statistic for the extension test. Therefore, when calculating TS_{ext} , we compare the likelihood fitting the source with an extended spatial model to the likelihood when fixing its extension to 10^{-10}° .

We estimate the error on the extension of a source by fixing the position of the source and varying the extension until the likelihood has fallen by $\frac{1}{2}$, corresponding to a 1σ error (Eadie et al. 1971). This method is shown schematically in Figure 1 which shows the change in the log of the likelihood when varying the extension of the SNR IC443. The localization error is calculated by fixing the extension and spectrum of the source and fitting to the likelihood function a 2D Gaussian as a function of position.

2.3. gtlike Analysis Validation

`pointlike` is important for LAT analyses that require many iterations such as source localization and extension fitting. On the other hand, because `gtlike` makes fewer approximations in calculating the likelihood we expect the spectral parameters found with `gtlike` to be slightly more precise. Furthermore, because `gtlike` is the standard likelihood analysis package, it has been more extensively validated for spectral analysis. For those reasons, in the following analysis we used `pointlike` to determine the position and extension of a source and subsequently derived the spectrum using `gtlike`. Both `gtlike` and `pointlike` can be used to estimate the statistical significance of the extension of a source and we required that both methods agree for a source to be considered extended. We found good agreement between the two methods. Unless explicitly mentioned, all TS, TS_{ext} , and spectral parameters were calculated using `gtlike` with the best-fit positions and extension found by `pointlike`.

2.4. Dual Localization

There is a degeneracy between a spatially extended source and multiple point sources separated by angular distances comparable to or smaller than the size of the LAT PSF. To assess the possibility of source confusion, we use `pointlike` to simultaneously fit the position of two point sources in the region of extended source candidates.

We define TS_{inc} as twice the increase in the log of the likelihood fitting the region as two point sources compared to fitting the region as one point source:

$$\text{TS}_{\text{inc}} = 2 \log(\mathcal{L}_{2\text{pts}}/\mathcal{L}_{\text{ps}}). \quad (6)$$

TS_{inc} can not be directly compared to TS_{ext} to see which model is more significant because the models are not nested (Protassov et al. 2002). Even though the comparison of TS_{ext} with TS_{inc} is not a calibrated test, we find the cases $\text{TS}_{\text{inc}} \ll \text{TS}_{\text{ext}}$ or $\text{TS}_{\text{inc}} \gg \text{TS}_{\text{ext}}$ suggestive and we only consider a source to be extended if $\text{TS}_{\text{ext}} > \text{TS}_{\text{inc}}$. Similar to the case of extended sources described in Section 2.3, the spectra of the two point sources can be refit using `gtlike`. We quote the spectral values obtained from `gtlike` using the best fit positions found using `pointlike`.

2.5. Comparing Source Sizes

We tested two different models for the surface brightness profile, either a 2D Gaussian

$$I(x, y) = \frac{1}{2\pi\sigma^2} \exp(-(x^2 + y^2)/2\sigma^2) \quad (7)$$

or a uniform disk

$$I(x, y) = \begin{cases} \frac{1}{\pi\sigma^2} & x^2 + y^2 \leq \sigma^2 \\ 0 & x^2 + y^2 > \sigma^2 \end{cases} \quad (8)$$

Although these shapes are significantly different, when convolved with the PSF, their profiles are very similar. This is demonstrated in Figure 2 by showing I_{src} , the PSF, and the PDF for a radially symmetric uniform brightness and a Gaussian surface brightness of size 0.5° .³ This plot shows that the LAT has little sensitivity to the exact structure of an extended source. Therefore, in our search for extended sources, we use only a uniform disk as our spatial extension shape. We then quote the radius of the disk edge as the size of the source.

3. Validation of Analysis Method

We test the false detection probability of `pointlike` by fitting the extension of point-like sources. Mattox et al. (1996) discuss that the test statistic distribution for a likelihood

³To allow a valid comparison between Gaussian and disk shaped morphologies, we define the source size for this test as the radius containing 68% of the intensity (r_{68}). $r_{68, \text{Gaussian}} = 1.51\sigma$ and $r_{68, \text{disk}} = 0.82\sigma$ where σ is defined in Equation 7 and Equation 8 respectively.

ratio test on the existence of a source at a given position is

$$P(\text{TS}) = \frac{1}{2}(\chi_1^2(\text{TS}) + \delta(\text{TS})). \quad (9)$$

The particular form of Equation 9 is due to the null hypothesis (source flux $\Phi = 0$) residing on the edge of parameter space and the model hypothesis adding a single degree of freedom. It is plausible to expect a similar distribution of the test statistic in the test for source extension since the same conditions apply (with the source flux Φ replaced by the source radius r and $r < 0$ being unphysical). To validate this claim, we performed Monte Carlo simulations to calculate empirical distributions for TS_{ext} and compared them to Equation 9.

We simulated point sources with various spectral forms using the LAT on-orbit simulation tool, `gtobssim`⁴ and fit them with `pointlike` using both point and extended source hypotheses. These point sources were simulated with a power-law spectral model with integrated fluxes above 100 MeV ranging from 3×10^{-9} to 1×10^{-6} ph cm⁻² s⁻¹ in six discrete steps and spectral indices ranging from 1.5 to 3 in four discrete steps. These values were picked to represent typical source parameters of LAT-detected sources. The point sources were simulated on top of an isotropic background with an integrated flux above 100 MeV of 1.5×10^{-5} ph cm⁻² s⁻¹ taken to be the same as the isotropic spectrum measured by EGRET (Sreekumar et al. 1998). The Monte Carlo simulation was performed over a one-year observation period using a representative rocking profile and a representative livetime fraction of 0.8. The reconstruction was performed using 1 GeV to 100 GeV photons and the Pass 7_V6 (P7_V6) Source Instrument Response Function (IRFs, Abdo et al. (2011a)). For each significantly detected point source ($\text{TS} \geq 25$), we used `pointlike` to fit it as an extended source and calculate TS_{ext} .

For each set of spectral parameters, $\sim 30,000$ statistically independent simulations were performed. For the dimmer spectral models, many of the simulations left the source undetected ($\text{TS} < 25$) and were discarded. Table 1 shows the different spectral models used in our study as well as the number of simulations. The cumulative density of TS_{ext} is plotted in Figure 3. The $\chi_1^2/2$ distribution of Equation 9 is overlaid for comparison.

Our study shows broad agreement between simulations and Equation 9. Nevertheless, the agreement is not perfect. It should be noted that the discrepancy seems to be worst for bright sources where numerical errors in the convolution are most apparent. Another possible reason for the departure from Equation 9 is that `pointlike` ignores energy dispersion which will change the PSF shape as a function of energy. We emphasize that many of the empirical distributions lie to the left of the theoretical curve so using the theoretical distribution will

⁴`gtobssim` is distributed publicly by the FSSC.

lead to an underestimate of the statistical significance of a detection. Therefore, we are confident that $\sqrt{\text{TS}_{\text{ext}}}$ can be used as a conservative measure of the statistical significance of a source’s extension and use it in the following analysis.

4. Extended Source Detection Threshold

We calculated the LAT’s detection threshold to detect that a spatially extended sources is extended. We define the detection threshold as the flux at which the value of TS_{ext} averaged over many statistical realizations of a source is $\langle \text{TS}_{\text{ext}} \rangle = 16$, corresponding to a 4σ detection (see section 3).

We used a simulation setup similar to that described in Section 3, but instead of point sources we simulated extended sources with a radially symmetric uniform surface brightness. Additionally, we simulated our sources over the two-year time range included in 2FGL. Each extension and spectral index, we selected a flux range which bracketed $\text{TS}_{\text{ext}} = 16$ and performed an extension test for > 100 independent realizations of ten flux values in this range. We calculated $\langle \text{TS}_{\text{ext}} \rangle = 16$ by fitting a line to the flux and TS_{ext} values in this narrow range.

Figure 4 shows the threshold for sources of four spectral indices from 1.5 to 3 and extension varying from $\sigma = 0^\circ.1$ to $2^\circ.0$. The LAT’s flux threshold for a significant detection of source extension drops quickly with increasing source size and reaches a minimum around $0^\circ.5$. Figure 4 shows the threshold using photons with energies between 100 MeV and 100 GeV and also using only 1 GeV to 100 GeV photons. Except for very large ($> 1^\circ$) sources, our detection threshold is not substantially improved by including photons with energies between 100 MeV and 1 GeV. This is also demonstrated in Figure 1 which shows TS_{ext} for the SNR IC443 computed independently in twelve energy bins between 100 MeV and 100 GeV. For IC443, which has a spectral index ~ 2.4 , almost the entire increase in likelihood modeling the source as being extended comes from energies above 1 GeV. On the other hand, other systematic errors become increasingly important at low energy. For our extension search, we therefore use only photons with energies above 1 GeV.

Figure 5 shows the flux threshold as a function of source extension for different background levels ($1\times$, $10\times$, and $100\times$ the nominal background), different spectral indices, and two different energy bands (1 GeV to 100 GeV and 10 GeV to 100 GeV). The detection threshold is higher for sources in regions of higher background. When studying sources only at energies above 1 GeV, the LAT’s detection threshold (defined as the 1 GeV to 100 GeV flux at which $\langle \text{TS}_{\text{ext}} \rangle = 16$) depends less strongly on the source’s spectral index. The index

dependence of the detection threshold is even weaker when considering only photons with energies above 10 GeV. Overlaid on Figure 5 are the LAT detected extended sources that will be discussed in Sections 6 and 8. The extension thresholds are tabulated in Table 2.

Finally, Figure 6 shows the LAT’s projected detection threshold to extension after 10 years against 10 times the isotropic background. This background is representative of the background near the Galactic plane. For small extended sources, our detection threshold improves by a factor larger than the square root of the exposure because at high energies, where we are most sensitive to extension, the background levels are in the Poisson instead of the Gaussian regime. For large extended sources, the relevant background is over a larger spatial range and so the improvement is closer to the expected factor corresponding to the square root of the exposure.

5. Extended Source Search Method

We test all sources in 2FGL for spatial extension. 2FGL included twelve previously published spatially extended sources but not attempt was made to fit the extension of these sources. Other than these sources, all 2FGL sources were modeled as point sources and 2FGL did not attempt to resolve the extension of new sources.

Our analysis technique is closely related to that of the 2FGL catalog. We used the same two-year dataset from 2008 August 4 to 2010 August 1 and we used the same P7_V6 Source class event selection and IRFs (Abdo et al. 2011a). The same models were used to describe the background from Galactic diffuse, isotropic, and Earth limb emission. To account for possible residuals in the diffuse emission model, the galactic emission was scaled by a power-law and the isotropic component’s normalization was left free.

As was shown in Section 4, we gain little in sensitivity using photons with energies below 1 GeV. On the other hand, the large PSF at low energy makes us more susceptible to systematic errors arising from source confusion due to multiple point sources and modeling of the Galactic diffuse emission. In addition, the Galactic diffuse emission is more pronounced at lower energies due to its steep energy spectrum (Abdo et al. 2009a). For that reason, we performed our search using only photons with energies between 1 GeV and 100 GeV.

We also performed a search for extended sources using only 10 GeV to 100 GeV photons. Even this approach tests the same sources, it is complimentary because the Galactic diffuse emission is even less dominant above 10 GeV. Furthermore, source confusion becomes less of a problem since most LAT sources are not significantly detected at energies exclusively above 10 GeV. So we expect to be able to resolve harder sources in more complicated regions. The

> 10 GeV analysis is especially beneficial for regions near pulsars which are not significantly detected above 10 GeV. A similar procedure was used to detect HESS J1825–137 and MSH 15–52 with the LAT (Abdo et al. 2010a; Grondin et al. 2011).

We tested each source for extension using `pointlike` assuming the source had a uniform radially symmetric surface brightness and a power-law spectral model. We used a circular 10 deg region of interest (ROI) centered on our source and included all catalog sources within 15 deg of the source of interest in our background model. We refit the spectral parameters of sources within 2 deg of the source to avoid potential biases of the extension parameters of the source of interest due to close-by background sources.

Finally, when analyzing each region, we automatically removed from our background model other 2FGL sources which were within 0.5° of the source of interest from the background model. This was done due to a concern that extended sources are included in 2FGL as multiple point sources. These spurious sources could distort the extension fit. Instead, when a source is found to be significantly extended (i.e. $\text{TS}_{\text{ext}} > 16$), we perform the dual localization procedure (described in Section 2.4 to compare the extended source hypothesis to the hypothesis of two independent point sources. Only sources with $\text{TS}_{\text{ext}} > \text{TS}_{\text{inc}}$ are considered as extended.

5.1. Additional Analysis

We expect most spatially resolvable extended sources to be located in our Galaxy and thus to be concentrated along the Galactic plane. Unfortunately, the GeV emission in the Galactic plane is dominated by extremely structured diffuse emission from the interactions of cosmic rays with the interstellar medium. Finding sources on top of this emission is difficult (Abdo et al. 2009b) as has been discussed in 1FGL and 2FGL (Abdo et al. 2010d, 2011b). Furthermore, the Galactic plane is crowded and it is often difficult to correctly model nearby sources. Because of this, finding a source with $\text{TS}_{\text{ext}} > 16$ is not a sufficient criteria alone for claiming a detection of source extension. For each extended source, we perform several analysis crosschecks.

For each candidate, we generated a map of residual TS by adding a new source of spectral index 2 into the region at each pixel and finding the increase in likelihood when fitting its flux. Residual TS maps are useful to look for residual structure in the sky model. Figure 7 shows a residual TS map for the extended source IC443. The residual TS map indicates that the spatially extended model for IC443 is a significantly better description of the observed photons. We also generated plots of the sum of all counts within a given

distance of the source and compared it to the model predictions of a point source. An example radial integral plot is shown for the extended source IC443 in Figure 1. For each source, we also made diffuse-emission-subtracted smoothed counts maps (show for IC443 in Figure 1).

We then inspected each extended source candidate to identify cases in which the extension fit is clearly influenced by large-scale residuals in the diffuse emission and hence the extension measurement is unreliable. An example of such a case is shown in Figure 8. It shows a Galactic and isotropic diffuse-emission-subtracted smoothed counts map of 2FGL J1856.2+0450c using 1 GeV to 100 GeV photons. In this region along the Galactic plane, there appears to be large-scale residual in the diffuse emission. As a result, 2FGL J1856.2+0450c is fit to an extension of 1.83° and the result is statistically significant with $\text{TS}_{\text{ext}} = 45.4$. However, by looking at the residuals it is clear that this complicated region is not fit well even though the source’s extension is statistically significant. We do not report sources that fail this inspection as extended.

For the remaining candidates, we took the spatial and spectral model found using `pointlike` and re-determined the spectral parameters using `gtlike`. We used the ‘binned likelihood’ mode of `gtlike` on a $14^\circ \times 14^\circ$ ROI with a pixel size of 0.03° . We obtained a second measure of TS_{ext} from `gtlike` for the extension and position of the source as determined by `pointlike`. We only considered a source to be significantly extended if $\text{TS}_{\text{ext}} > 16$ with both `pointlike` and `gtlike`.

Because of the high source density in the Galactic plane, we often had to iteratively improve the model of our background sources to obtain a better fit of the candidate source. Several catalog sources would often fill in the emission of the extended source and had to be removed from the background model of the region. Similarly, background sources were often insignificant in the fit energy range and had to be removed from the sky model. The position of background sources would often have to be refit once the extended source was fit. When the model of the extended source coupled strongly with nearby sources, we iteratively fit the extended source and all nearby sources until the fit converged. For each extended source, we describe the modifications of the background model compared to the model used in the creation of the 2FGL catalog that were required.

5.2. Systematic Errors on Extension

We estimate a systematic error on the extension of a source due to uncertainty in our knowledge of the LAT PSF. Before launch, the LAT PSF was determined by detector simu-

lations which were verified in accelerator tests (Atwood et al. 2009). However, in-flight data revealed a discrepancy above a few GeV in the PSF compared to the angular distribution of photons from bright AGN. A publication on this issue is in preparation (Abdo et al. 2011a). Subsequently, the PSF was fit empirically to bright AGN and this empirical parameterization is the default PSF used in the P7_V6 IRFs. To account for this uncertainty in our knowledge of the PSF, we refit our extended source candidates using the pre-flight Monte Carlo representation of the PSF and consider the difference in extension found using the two PSFs as a systematic error on the extension of a source. The same approach was used in (Abdo et al. 2010h). At high energies, we believe that our parameterization of the PSF from bright AGN is substantially better than the Monte Carlo representation of the PSF so this estimate of systematic errors is conservative.

We estimate a second systematic error on the extension of a source due to uncertainty in the model of the Galactic diffuse emission by using an alternative diffuse model. An alternative model was based upon GALPROP⁵ and used in the LAT analysis of the isotropic diffuse emission (Abdo et al. 2010j). The intensities of various components to the galactic diffuse emission were then fitted individually using a spatial distribution of the intensities within the ROI as predicted by the model. We distinguish contributions from CR interactions with the molecular hydrogen, the atomic+ionized hydrogen, residual gas traced by dust (Grenier et al. 2005), and the interstellar radiation field. We further split the contributions from interactions with molecular and atomic hydrogen to the Galactic diffuse emission according to the distance from the Galactic center in which they are produced. Hence, we replace the standard diffuse emission model by 18 individually fitted templates to describe individual components of the diffuse emission. A similar crosscheck was used in the LAT Collaboration’s analysis of RX J1713.7–3946 (Abdo et al. 2011c).

It is not expected that this diffuse model is superior to the standard LAT model obtained through an all-sky fit. However, adding degrees of freedom to the background model can remove likely spurious sources that correlate with features in the Galactic diffuse emission. Therefore, this tests systematics that may be due to incorrect modeling of the diffuse emission in the region.

We do not except the systematic error due to uncertainties in the PSF to be correlated to the systematic due to uncertainty in the Galactic diffuse emission so the total systematic error on the extension of a source so we obtain the total systematic error by adding them in quadrature.

⁵GALPROP is a software package for calculating the Galactic γ -ray emission based on a model of cosmic-ray propagation in the Galaxy. See <http://galprop.stanford.edu/> for details and references

6. Analysis of Extended Sources Identified in 2FGL

We first present on our analysis of the twelve extended sources included in 2FGL (Abdo et al. 2011b). Six extended SNRs were included in 2FGL: W51C, IC443, W28, W30, W44, and the Cygnus Loop (Abdo et al. 2009c, 2010h,e,g; Katagiri et al. 2011).⁶ GeV emission from W30 was also studied in Castro & Slane (2010). Using 1 GeV to 100 GeV photons, our analysis significantly detected the extension of all six SNRs.

Two nearby satellite galaxies of the Milky Way the Large Magalenic Cloud (LMC) and the Small Magalenic Cloud (SMC) were included in 2FGL as spatially extended sources (Abdo et al. 2010i,b). They were significantly detected using 1 GeV to 100 GeV photons. Our fit extension is comparable to the published result, but we note that previous LAT Collaboration publication on LMC used a more complicated two 2D Gaussian surface brightness spatial model when fitting it ((Abdo et al. 2010i)).

Three PWNe, MSH 15–52, Vela X, and HESS J1825–137 were identified in 2FGL (Abdo et al. 2010a,f; Grondin et al. 2011). HESS J1825–137 was significantly detected using 10 GeV to 100 GeV photons. To improve the model of this source, we removed from our background model the nearby catalog source 2FGL J1823.1–1338c which is part of the extended source. To avoid confusion with the nearby bright pulsar PSR J1509–5850, MSH 15–52 must be analyzed at high energies. Using photons with energies above 10 GeV, we fit the extension of MSH 15–52 to be consistent with the published size with an extension significance of $TS_{\text{ext}} = 6.5$.

Our analysis was unable to resolve Vela X which would have required first removing the pulsed photons from the Vela pulsar which is beyond the scope of this paper. Our analysis also failed to detect a significant extension for the Centaurus A Lobes (Abdo et al. 2010c). This is because the source’s emission is significantly different from a uniform radially symmetric surface brightness.

Our analysis of these sources is summarized in Table 3. This table includes the best fit position and extension of these sources when fitting them as disk-shaped sources with a radially symmetric uniform surface brightness. It also includes the best fit spectral parameters for each source. The position and extension of Vela X and the Centaurus A Lobes are taken from Abdo et al. (2010f,c) and are included in this list for completeness.

⁶A detailed publication by the LAT Collaboration about W30 is still in preparation.

7. Test of 2LAC Sources

To validate our method, we test LAT sources associated with AGN for extension. GeV emission from AGN is believed to originate from the cores of kiloparsec-scale jets of distant galaxies. Therefore AGN are not expected to be spatially resolvable by the LAT and provide a good calibration source to demonstrate that our extension detection method does not misidentify point sources as being extended. We note that megaparsec-scale γ -ray halos around AGNs have been hypothesized (Aharonian et al. 1994) to be resolvable by the LAT. However, no such halo has been discovered in the LAT data so far.

Following 1FGL, the LAT Collaboration published the First LAT AGN Catalog (1LAC), a list of sources that had a high probability association with AGN (Abdo et al. 2010k). 1FGL had 709 1FGL sources associated with 671 distinct AGN at high latitude ($|b| > 10$ deg). Using two years of data and 2FGL, the Second LAT AGN Catalog (2LAC) associated 1016 2FGL sources with AGN (Ackermann et al. 2011). To avoid systematic problems with AGN classification, we selected 885 out of the 1016 AGN which made it into the clean AGN sub-sample. An AGN association is considered clean only if it has a high probability of association $P \geq 80\%$, if it is the only AGN associated with the catalog source, and if there are no flags on the source in 2FGL. These last two conditions are important for our analysis. Source confusion may look like a spatially extended source and flagged catalog sources may correlate with unmodeled structure in the diffuse emission.

Of the 885 clean AGN, we select 783 of these 2FGL sources which are significantly-detected above 1 GeV and fit each of them for extension. A histogram of the TS_{ext} values computed for these AGN is shown in Figure 9. Overlaid on the plot is the $\chi^2/2$ distribution of Equation 9. The TS_{ext} distribution for AGN shows good agreement with the theoretical distribution. Two sources had $\text{TS}_{\text{ext}} > 10$. One was due to the incorrect removal of a nearby catalog sources from the sky model (see Section 5) and the other was due to a failure of convergence of the point hypothesis. This result demonstrates that we can use TS_{ext} as a measure of the statistical significance of the detection of the extension of a source.

We should clarify that the LAT PSF used in this study was determined empirically by fitting the observed shape of bright AGN (see Section 5.2). Finding that the AGN we test are not extended is not surprising. This validation analysis is not suitable to reject any hypotheses about the existence of megaparsec-scale halos around AGN.

8. New Extended Sources

Nine extended sources not included in 2FGL were found using this search. Three were found in our search using 1 GeV to 100 GeV photons and six were found in our search using 10 GeV to 100 GeV photons. The fit properties of these nine sources is summarized in Table 4. This table includes for each source the best fit position, extension, spectrum, source significance, and significance of extension.

The results of our investigation of systematic uncertainties of this measurement are presented in Table 5. It shows a comparison between the fit with a single extended source hypothesis and the fit assuming the emission originates from two independent sources and the results of the extension fit using variations of the PSF and the galactic diffuse model described in Section 5.2. There is good agreement between TS_{ext} and the fit size using the standard analysis, the alternative diffuse models, and the alternative PSF. This suggests that the sources are robust against features in the diffuse model and uncertainties in the angular resolution.

8.1. 2FGL J0823.0–4246

The source 2FGL J0823.0–4246 was found to have an extension of $0^\circ 37 \pm 0^\circ 03_{\text{stat}} \pm 0^\circ 02_{\text{sys}}$ with an extension significance of $TS_{\text{ext}} = 46.3$ using 1 GeV to 100 GeV photons. This source was fit to a position of $(l, b) = (260^\circ 32, -3^\circ 28)$. This source is coincident with the one-year catalog source 1FGL J0823.3–4248. Figure 10 shows a counts map of this source and Figure 18 shows its spectrum. To get a good fit of this source, we removed from our background model the nearby catalog sources 2FGL J0823.4–4305 and 2FGL J0821.0–4254 which are part of the extended source. These modifications are shown in Figure 10.

This extended source is spatially coincident with the middle-aged SNR Puppis A. Puppis A has been studied in detail in radio (Castelletti et al. (2006), and references therein) and X-ray (Petre et al. (1996); Hwang et al. (2008), and references therein) Mosaic *ROSAT* observations of Puppis A produced the highest resolution X-ray image of this source and contours corresponding to this image are overlaid on Figure 10 and match the inferred size at GeV energies (Petre et al. 1996). Puppis A’s distance was estimated at 2.2 kpc (Reynoso et al. 1995, 2003) which leads to a 1 GeV to 100 GeV luminosity of $\sim 3 \times 10^{34}$ ergs/s. No molecular clouds have been observed directly adjacent to Puppis A (Paron et al. 2008). This is similar to the LAT detected Cyngus Loop SNR (Katagiri et al. 2011). The luminosity of Puppis A is also smaller than that of other SNRs believed to interact with molecular clouds (Abdo et al. 2009c, 2010h,g,e; The Fermi-LAT Collaboration 2010). (Katagiri et al. 2011).

8.2. 2FGL J1627.0–2425c

The source 2FGL J1627.0–2425c was found to have an extension of $0^\circ.41 \pm 0^\circ.05_{\text{stat}} \pm 0^\circ.02_{\text{sys}}$ with an extension significance of $\text{TS}_{\text{ext}} = 31.1$ using 1 GeV to 100 GeV photons. The best fit position is $(l, b) = (353^\circ.08, 16^\circ.78)$. This source is coincident with the one year catalog source 1FGL J1628.6–2419c. A counts map showing this source is seen in Figure 11.

This source is in a region of remarkably complicated diffuse emission. Even though it is 16 deg from the Galactic plane, this source is on top of the core of the Ophiuchus molecular cloud which contains massive star-forming regions that are bright in the infrared. The region also has abundant molecular and atomic gas traced by CO and HI but also plenty of dark gas found only by its association with dust emission (Grenier et al. 2005). Embedded star-forming regions make it even more challenging to measure the column density of dust. Infrared and ^{12}CO ($J = 1 \rightarrow 0$) contours are overlaid on Figure 11. There is good spatial correlation with the GeV emission (Young et al. 1986; de Geus et al. 1990) so this source might represent γ -ray emission from the interactions of cosmic rays with interstellar gas which has not been accounted for in the LAT diffuse emission model.

8.3. 2FGL J1712.4–3941

The source 2FGL J1712.4–3941 was found photons to have an extension $0^\circ.56 \pm 0^\circ.04_{\text{stat}} \pm 0^\circ.02_{\text{sys}}$ with an extension significance of $\text{TS}_{\text{ext}} = 39.6$ using 1 GeV to 100 GeV. This source was fit to a position of $(l, b) = (347^\circ.25, -0^\circ.54)$. this source is coincident with the one-year catalog source 1FGL J1711.7–3944c. Figure 12 shows a smoothed counts map of this source.

This source is spatially coincident with the SNR RX J1713.7–3946 and was recently reported by (Abdo et al. 2011c). Figure 12 overlays H.E.S.S. TeV contours of SNR RX J1713.7–3946 from (Aharonian et al. 2007b). To analyze this source, we used the same background model as the recent LAT publication. 2FGL J1715.4–4024c is spatially coincident with Source A and was moved to $(\text{RA}, \text{Dec}) = (258.84, -40.46)$. Source B was added at $(\text{RA}, \text{Dec}) = (258.71, -38.70)$ and Source C was added at $(\text{RA}, \text{Dec}) = (257.47, -39.75)$.

8.4. 2FGL J0851.7–4635

The source 2FGL J0851.7–4635 was found to have an extension of $1^\circ.13 \pm 0^\circ.08_{\text{stat}} \pm 0^\circ.05_{\text{sys}}$ with an extension significance of $\text{TS}_{\text{ext}} = 87.2$ using 10 GeV to 100 GeV photons. This source was fit to a position of $(l, b) = (266^\circ.29, -1^\circ.43)$. Figure 13 shows a counts map of this source.

2FGL J0851.7–4635 is spatially coincident with the SNR Vela Jr. Overlaid on Figure 13 are contours of Vela Jr. as seen in TeV by H.E.S.S (Aharonian et al. 2007a). The GeV and TeV morphology match well. A detailed papers by the LAT Collaboration on Vela Jr. is in preparation.

To get a good fit of this source, removed from our background model the nearby catalog sources 2FGL J0853.5–4711, 2FGL J0848.5–4535, and 2FGL J0855.4–4625 which are part of the extended source. In addition, we relocalized the position of the nearby catalog source 2FGL J0854.7–4501 to $(l, b) = (266^\circ 24', 0^\circ 49')$ to better fit its position at high energies in the presence of the extended source. In addition, we removed from our model the further away catalog sources 2FGL J0858.0–4815 and 2FGL J0901.7–4655 because they were not significant above 10 GeV.

8.5. 2FGL J1615.0–5051

The source 2FGL J1615.0–5051 was found photons to have an extension of $0^\circ 33' \pm 0^\circ 04'_{\text{stat}} \pm 0^\circ 01'_{\text{sys}}$ with an extension significance of $\text{TS}_{\text{ext}} = 16.3$ using 10 GeV to 100 GeV. This source was fit to a position of $(l, b) = (332^\circ 38', -0^\circ 14')$. This source is coincident with the one-year catalog source 1FGL J1613.6–5100c. Figure 14 shows a counts map of this source.

This source is less than 1 deg away from 2FGL J1615.2–5138 which is also spatially extended (see Section 8.6). To get a good fit of both sources, we modeled both sources as being spatially extended and iteratively fit the position and extension of each source until obtaining a global best fit. Before doing this, We removed from our background model the source 2FGL J1614.9–5212 because it is part of 2FGL J1615.2–5138’s. Furthermore, we removed from our model the nearby catalog sources 2FGL J1619.7–5040c and 2FGL J1620.6–5111c because they were not significant above 10 GeV. These modifications are further described in the caption to Figure 14.

2FGL J1615.2–5138 is spatially coincident with the extended TeV source HESS J1616–508 (Aharonian et al. 2006). In Figure 14, contours of HESS J1616–508 are overlaid on 2FGL J1615.0–5051. The H.E.S.S. experiment measured an extension 0.136 ± 0.008 when fitting this source with an elliptical 2D Gaussian surface brightness. This size corresponds to a 68% containment radius of $r_{68} = 0^\circ 21' \pm 0^\circ 01'$. This size is comparable to the LAT size $r_{68} = 0^\circ 27' \pm 0^\circ 03'$ (see Section 2.5). Figure 19 shows that the spectrum of 2FGL J1615.0–5051 at GeV energies connects smoothly to the spectrum of HESS J1616–508 at TeV energies.

HESS J1616–508 is located in the region of two SNRs, RCW103 (G332.4-04) and

Kes 32 (G332.4+0.1) but is not spatially coincident with either of them (Aharonian et al. 2006). HESS J1616–508 is near three pulsars PSR J1614–5048, PSR J1616–5109, and PSR J1617–5055 but only PSR J1617–5055 is energetically favored as being the TeV emitter (Torii et al. 1998; Landi et al. 2007a). Aharonian et al. (2006) speculated that a PWN powered by this young pulsar could be responsible for the emission of HESS J1616–508. Because HESS J1616–508 is $9'$ away from PSR J1617–5055, this would require an asymmetric X-ray PWNe to power the TeV emission. However, *Chandra* ACIS observations revealed only an underluminous PWN of about $\sim 1'$ size around the pulsar which was not oriented towards the TeV emission, rendering this association as uncertain (Kargaltsev et al. 2009). No other promising counterparts were observed in observations of X-ray and soft gamma-ray emission by *Suzaku* (Matsumoto et al. 2007), *Swift*/XRT, IBIS/ISGRBI, BeppoSAX and *XMM-Newton* (Landi et al. 2007a). Finally, Kargaltsev et al. (2009) found diffuse emission towards the center of HESS J1616–508 using archival radio and infrared observations. Deeper observations will likely be necessary to understand this region.

8.6. 2FGL J1615.2–5138

The source 2FGL J1615.2–5138 was found photons to have an extension of $0^\circ.42 \pm 0^\circ.03_{\text{stat}} \pm 0.01_{\text{sys}}$ with an extension significance of $\text{TS}_{\text{ext}} = 48.0$ using 10 GeV to 100 GeV. This source was fit to a position of $(l, b) = (331^\circ.66, -0^\circ.66)$. This source is coincident with the one-year catalog source 1FGL J1614.7–5138c. Because 2FGL J1615.2–5138 is close to 2FGL J1615.0–5051, the same model described in Section 8.5 was used to analyze both sources. Both sources can be seen in Figure 14.

This source is spatially coincident with the extended TeV source HESS J1614–518 (Aharonian et al. 2006). In Figure 14, contours of HESS J1614–518 are overlaid on 2FGL J1615.2–5138. The H.E.S.S. experiment measured a 2D Gaussian extension of $\sigma = 0^\circ.23 \pm 0^\circ.02$ and $\sigma = 0.15 \pm 0.02$ in the semi-major and semi-minor axis. This size corresponds to a 68% containment size of $r_{68} = 0^\circ.35 \pm 0^\circ.03$ and 0.23 ± 0.03 . This elliptical size matches the LAT size $r_{68} = 0^\circ.35 \pm 0^\circ.03$. Figure 19 shows that the spectrum of 2FGL J1615.2–5138 at GeV energies connects smoothly to the spectrum of HESS J1614–518 at TeV energies. Further data collected by H.E.S.S. in 2007 helped to resolve a double peaked structure in the H.E.S.S. data but no spectral variation across this source, suggesting that the emission is not the confusion of physically separate sources (Rowell et al. 2008). The source was also detected by CANGAROO-III (Mizukami et al. 2011).

There are five nearby pulsars, but none are luminous enough to provide the energy output required to power the TeV emission (Rowell et al. 2008). HESS J1614–518 is spatially

coincident with a young open cluster Pismis 22 (Landi et al. 2007b; Rowell et al. 2008). *Suzaku* detected two promising X-ray candidates. Source A is an extended source consistent with the peak of HESS J1614–518 and source B coincident with Pismis 22 and towards the center but in a relatively dim region of HESS J1614–518 (Matsumoto et al. 2008). Three hypothesis have been presented to explain this emission; either source A is an SNR powering the γ -ray emission, source A is a PWN powered by an undiscovered pulsar in either source A or B, and finally that the emission may arise from hadronic acceleration in the stellar winds of Pismis 22 (Mizukami et al. 2011).

8.7. 2FGL J1632.4–4753c

The source 2FGL J1632.4–4753c was found to have an extension of $0^\circ.44 \pm 0^\circ.04_{\text{stat}} \pm 0^\circ.03_{\text{sys}}$ with an extension significance of $\text{TS}_{\text{ext}} = 64.5$ using 10 GeV to 100 GeV photons. This source was fit to a position of $(l, b) = (336^\circ.41, 0^\circ.22)$. This source is coincident with the one year catalog source 1FGL J1632.9–4802c. Figure 15 shows a counts map of this source.

To get a good fit of this source, we removed from our background model three catalog sources 2FGL J1631.7–4720c, 2FGL J1630.2–4752, 2FGL J1634.4–4743c.4–4820c that were part of the extended source.. We then iteratively relocalized the source 2FGL J1635.4–4717c to $(l, b) = (337^\circ.23, 0^\circ.35)$ and 2FGL J1636.3–4740c to $(l, b) = (336^\circ.97, -0^\circ.07)$ while fitting the extension of 2FGL J1632.4–4753c. In addition we removed from our model four farther away two-year catalog sources 2FGL J1638.0–4703c, 2FGL J1628.1–4857c, 2FGL J1630.1–4615, 2FGL J1639.8–4921c because they were not significant above 10 GeV. These modifications are shown in Figure 15.

This extended source is spatially coincident with the extended TeV source HESS J1632–478 (Aharonian et al. 2006). In Figure 15, contours of HESS J1632–478 are overlaid on 2FGL J1635.4–4717c. H.E.S.S. measured a extension of $\sigma = 0.21 \pm 0.05$ and 0.06 ± 0.04 along the semi-major and semi-minor axes when fitting this source with an elliptical 2D Gaussian surface brightness. This corresponds to a 68% containment size $r_{68} = 0^\circ.31 \pm 0^\circ.08$ and $0^\circ.09 \pm 0^\circ.06$ along the semi-major and semi-minor axis. This size is consistent with the LAT size $r_{68} = 0^\circ.36 \pm 0^\circ.04$. Figure 19 shows that the spectrum of 2FGL J1635.4–4717c at GeV energies connects smoothly to the spectrum of HESS J1632–478 at TeV energies.

Aharonian et al. (2006) argued that HESS J1632–478 is positionally coincident with the hard X-ray source IGR J1632-4751 observed by INTEGRAL, *XMM-Newton*, and *ASCA* (Tomsick et al. 2003; Rodriguez et al. 2003; Sugizaki et al. 2001), but this source is suspected to be a galactic X-Ray Binary so the γ -ray extension disfavors the association. Further obser-

variations by *XMM-Newton* reveal extended emission of size $\sim 32'' \times 15''$ and inside point-like emission coincident with the peak H.E.S.S. emission (Balbo et al. 2010). They found in archival MGPS-2 data a spatially coincident extended radio source (Murphy et al. 2007). The positional match argues for a single synchrotron process producing X-ray and GeV and TeV radiation, likely due to a PWNe. The increased size at TeV energies compared to X-ray energies has previously been observed in several aging PWNe including HESS J1825–137 (Gaensler et al. 2003; Aharonian et al. 2006b), HESS J1640–465 (Aharonian et al. 2006; Funk et al. 2007), and Vela X (Markwardt & Ogelman 1995; Aharonian et al. 2006c). This can be explained by a different synchrotron cooling time for the electrons producing X-rays and TeV γ -rays.

8.8. 2FGL J1837.3–0700c

The source 2FGL J1837.3–0700c was found to have an extension of $0^\circ 35 \pm 0^\circ 08_{\text{stat}} \pm 0^\circ 03_{\text{sys}}$ with an extension significance of $\text{TS}_{\text{ext}} = 18.8$ using 10 GeV to 100 GeV photons. This source was fit to a position of $(l, b) = (25^\circ 08, 0^\circ 13)$. This source is coincident with the one year catalog source 1FGL J1837.5–0659c. Figure 16 shows a counts map of this source.

This source is in a complicated region. There are three nearby catalog sources 2FGL J1834.7–0705c, 2FGL J1836.8–0623c, and 2FGL J1839.3–0558c. To get a good fit of 2FGL J1837.3–0700c, we relocalized 2FGL J1834.7–0705c to $(l, b) = (24^\circ 77, 0^\circ 50)$, 2FGL J1836.8–0623c to $(l, b) = (25^\circ 57, 0^\circ 32)$, and 2FGL J1839.3–0558c to $(l, b) = (26^\circ 08, 0^\circ 23)$. We removed from our background model the nearby catalog source 2FGL J1835.5–0649 which is part of the extended source and also the farther away catalog source 2FGL J1839.0–0539 because it was not significant above 10 GeV. These modifications are shown in Figure 16.

This source is spatially coincident with the TeV source HESS J1837–069 (Aharonian et al. 2006). In Figure 16, contours of HESS J1837–069 are overlaid on 2FGL J1837.3–0700c. H.E.S.S. measured an extension of $\sigma = 0.12 \pm 0.02$ and 0.05 ± 0.02 along the semi-major and semi-minor axis when fitting this source with an elliptical 2D Gaussian surface brightness. This corresponds to a 68% containment radius of $r_{68} = 0^\circ 18 \pm 0^\circ 03$ and $0^\circ 08 \pm 0^\circ 03$ along the semi-major and semi-minor axis. The size is comparable to LAT which fit a 68% containment radius of $r_{68} = 0^\circ 29 \pm 0^\circ 07$. the size difference is not significant (less than 2 sigma). Figure 19 shows that the spectrum of 2FGL J1837.3–0700c at GeV energies connects smoothly to the spectrum of HESS J1837–069 at TeV energies.

HESS J1837–069 is coincident with the hard and steady X-ray source AX J1838.0–0655 (Hertz & Grindlay 1988; Bamba et al. 2003; Malizia et al. 2005; Landi et al. 2006; Gotthelf & Halpern

2008; Anada et al. 2009). This source was discovered by RXTE to be a pulsar sufficiently luminous to power the TeV emission. AX J1838.0–0655 was spatially resolved by *Chandra* to be a bright point source surrounded by a $\sim 2'$ nebula (Gotthelf & Halpern 2008) and so the γ -ray emission may be powered by this pulsar. A second X-ray point source AX J1837.3–0652 is in the region of HESS J1837–069 (Bamba et al. 2003; Landi et al. 2006; Gotthelf & Halpern 2008; Anada et al. 2009). It was also resolved into point-like and diffuse component although no pulsations have yet been detected from it (Gotthelf & Halpern 2008). If AX J1838.0–0655 is a pulsar/PWN powering HESS J1837–069, some of the TeV emission may also come from AX J1837.3–0652.

8.9. 2FGL J2021.5+4026

The source 2FGL J2021.5+4026 was found to have an extension of $0^\circ 59 \pm 0^\circ 03_{\text{stat}} \pm 0^\circ 02_{\text{sys}}$ with an extension significance of $\text{TS}_{\text{ext}} = 116.4$ using 10 GeV to 100 GeV photons. This source was fit to a position of $(l, b) = (78^\circ 18, 2^\circ 19)$. This source is coincident with the one-year catalog source 1FGL J2020.0+4049. Figure 17 shows a counts map of this source and Figure 18 shows its spectrum.

To get a good fit of this source, we removed from our background model the nearby catalog source 2FGL J2019.1+4040 which were part of the extended source. Further, we found it necessary to add an additional point source not in the two-year catalog into our background model. The new source is localized to a position of $(l, b) = (78^\circ 85, 2^\circ 67)$ and had $\text{TS} = 13.5$. Although this source is not very significant, not including it into the background model significantly biased the fit extension. In addition, we removed from our model the four further away catalog sources 2FGL J2022.8+3843c, 2FGL J2020.0+4159, 2FGL J2013.8+4115c, and 2FGL J2012.4+3955c from the region because they were not significant above 10 GeV. These modifications are further described in the caption to Figure 17.

This extended sources is coincident with 2CG 078+01 and 3EG J2020+4017 detected by COS B and EGRET respectively (Swanenburg et al. 1981; Hartman et al. 1999). This source is spatially coincident with the γ -Cygni SNR and has been speculated to originate from the interaction of accelerated particles in the SNR interacting with dense molecular clouds (Pollock 1985; Gaisser et al. 1998). But this association was disfavored when the LAT GeV emission from this source was detected to be pulsed (PSR J2021+4026, Abdo et al. (2010)).

Milagro detected a 4.2σ excess at energies $\sim 30\text{TeV}$ from the location of this source in the previous LAT bright γ -ray source list. Abdo et al. (2009d,e). Veritas also detected an extended source VER J2019+407 coincident with the SNR above 200 GeV and suggested

the TeV emission could be a shock-cloud interaction in γ -Cygni (Weinstein 2009). Using just 10 GeV to 100 GeV photons to avoid PSR J2021+4026, we resolve an extended source whose inferred size at GeV energies well matches the radio size of γ -Cygni, as can be seen in Figure 17 which overlays contours of γ -Cygni at 408MHz from the Canadian Galactic Plane Survey (Taylor et al. 2003).

9. Discussion

Twelve extended sources were included in 2FGL. Using two years of LAT data and a new analysis method, we presented the detection of nine additional extended sources. We also reanalyze the spatial shape of the twelve extended sources in 2FGL. The 21 extended LAT sources are located close to the Galactic plane and their localizations shown in Figure 20. Most of the extended sources are indeed expected to be of Galactic origin as the distance of extragalactic sources (with the exception of the local group Galaxies) is typically too large to resolve them in γ -rays.

For the LAT extended sources also seen in the TeV energy range, Figure 21 shows that there is a good correlation between the size of the sources in the GeV and TeV energy ranges. Even so, the size of PWNe are expected to vary across the GeV and TeV energy range and the size of HESS J1825–137 is significantly larger at GeV than TeV energies (Grondin et al. 2011). It is interesting to compare the size at GeV and TeV energies of other PWN candidates, but definitively measuring this would require a more in-depth analysis of the LAT data using the same elliptical surface brightness model.

Figure 22 compares the size of the 21 extended LAT sources to the 42 extended H.E.S.S. sources.⁷ Because of the large field of view and all-sky coverage, the LAT can more easily measure larger sources including the LMC and SMC. On the other hand, the better angular resolution of Air Cherenkov detectors allows them to measure a population of extended sources below our sensitivity limit (currently at about $\sim 0^\circ.2$). *Fermi* has a five year nominal mission lifetime with a goal of ten years of operation. As Figure 6 shows, the LAT’s low background at high energies will allow its sensitivity to these smaller sources to improve by a factor greater than the square root of the exposure. With increased exposure, the LAT will likely begin to detect and resolve many smaller TeV sources.

Figure 23 compares the spectral index of LAT detected extended sources and of all

⁷The TeV extension of the 42 extended H.E.S.S. sources comes from the H.E.S.S. Source Catalog. The H.E.S.S. source catalog can be found at <http://www.mpi-hd.mpg.de/hfm/HESS/pages/home/sources/>.

sources in 2FGL. This, and Table 3 and 4, show that the LAT observes a population of hard extended sources at energies above 10 GeV. Figure 19 shows that the spectra of four of these sources (2FGL J1615.0–5051, 2FGL J1615.2–5138, 2FGL J1632.4–4753c, and 2FGL J1837.3–0700c) at GeV energies connect smoothly to their H.E.S.S. counterparts at TeV energies. This is also true of Vela Jr., HESS J1825–137 (Grondin et al. 2011), RX J1713.7–3946 (Abdo et al. 2011c). It is likely that the GeV and TeV emission from these sources originates from the same population of high-energy particles.

Many of the TeV detected extended sources now seen at GeV energies are currently unidentified and further multi-wavelength follow-up observations will be necessary to understand these particle accelerators. But the extension of the spectrum of these TeV sources towards lower energies by LAT observations can help to determine the origin and nature of the high-energy emission seen from these sources.

REFERENCES

- Abdo, A. A., et al. 2009a, *Physical Review Letters*, 103, 251101
- . 2009b, *Physical Review Letters*, 103, 251101
- . 2009c, *ApJ*, 706, L1
- . 2009d, *ApJS*, 183, 46
- . 2009e, *ApJ*, 700, L127
- . 2009f, *Astroparticle Physics*, 32, 193
- . 2010a, *ApJ*, 714, 927
- . 2010b, *A&A*, 523, A46+
- . 2010c, *Science*, 328, 725
- . 2010d, *ApJS*, 188, 405
- . 2010e, *ApJ*, 718, 348
- . 2010f, *ArXiv e-prints*
- . 2010g, *Science*, 327, 1103
- . 2010h, *ApJ*, 712, 459

- 718 —. 2010i, A&A
- 719 —. 2010j, Physical Review Letters, 104, 101101
- 720 —. 2010k, ApJ, 715, 429
- 721 —. 2010l, ApJS, 187, 460
- 722 —. 2011a, Astroparticle Physics, in preparation
- 723 —. 2011b, ArXiv e-prints
- 724 —. 2011c, ApJ, 734, 28
- 725 Acciari, V. A., et al. 2009, ApJ, 698, L133
- 726 —. 2011, ArXiv e-prints
- 727 Ackermann, M., et al. 2011, ArXiv e-prints
- 728 Aharonian, F., et al. 2005, A&A, 435, L17
- 729 —. 2006a, A&A, 460, 743
- 730 —. 2006b, A&A, 460, 365
- 731 —. 2006c, A&A, 448, L43
- 732 Aharonian, F., et al. 2006, ApJ, 636, 777
- 733 Aharonian, F., et al. 2007a, ApJ, 661, 236
- 734 —. 2007b, A&A, 464, 235
- 735 —. 2008, A&A, 481, 401
- 736 Aharonian, F. A., Coppi, P. S., & Voelk, H. J. 1994, ApJ, 423, L5
- 737 Aharonian, F. A., et al. 2007c, A&A, 469, L1
- 738 Albert, J., et al. 2006, Science, 312, 1771
- 739 Anada, T., Ebisawa, K., Dotani, T., & Bamba, A. 2009, PASJ, 61, 183
- 740 Atwood, W. B., et al. 2009, ApJ, 697, 1071

- 741 Balbo, M., Saouter, P., Walter, R., Pavan, L., Tramacere, A., Pohl, M., & Zurita-Heras,
742 J.-A. 2010, *A&A*, 520, A111+
- 743 Baltz, E. A., et al. 2008, *J. Cosmology Astropart. Phys.*, 7, 13
- 744 Bamba, A., Ueno, M., Koyama, K., & Yamauchi, S. 2003, *ApJ*, 589, 253
- 745 Blandford, R., & Eichler, D. 1987, *Phys. Rep.*, 154, 1
- 746 Castelletti, G., Dubner, G., Golap, K., & Goss, W. M. 2006, *A&A*, 459, 535
- 747 Castro, D., & Slane, P. 2010, *ApJ*, 717, 372
- 748 Dame, T. M. 2011, *ArXiv e-prints*
- 749 de Geus, E. J., Bronfman, L., & Thaddeus, P. 1990, *A&A*, 231, 137
- 750 Eadie, W. T., Drijard, D., & James, F. E. 1971, *Statistical methods in experimental physics*,
751 ed. Eadie, W. T., Drijard, D., & James, F. E.
- 752 Funk, S., Hinton, J. A., Pühlhofer, G., Aharonian, F. A., Hofmann, W., Reimer, O., &
753 Wagner, S. 2007, *ApJ*, 662, 517
- 754 Gaensler, B. M., Schulz, N. S., Kaspi, V. M., Pivovarov, M. J., & Becker, W. E. 2003, *ApJ*,
755 588, 441
- 756 Gaisser, T. K., Protheroe, R. J., & Stanev, T. 1998, *ApJ*, 492, 219
- 757 Górski, K. M., Hivon, E., Banday, A. J., Wandelt, B. D., Hansen, F. K., Reinecke, M., &
758 Bartelmann, M. 2005, *ApJ*, 622, 759
- 759 Gotthelf, E. V., & Halpern, J. P. 2008, *ApJ*, 681, 515
- 760 Grenier, I. A., Casandjian, J.-M., & Terrier, R. 2005, *Science*, 307, 1292
- 761 Grondin, M. ., et al. 2011, *ArXiv e-prints*
- 762 Hartman, R. C., et al. 1999, *ApJS*, 123, 79
- 763 Hertz, P., & Grindlay, J. E. 1988, *AJ*, 96, 233
- 764 Hwang, U., Petre, R., & Flanagan, K. A. 2008, *ApJ*, 676, 378
- 765 James, F., & Roos, M. 1975, *Comput. Phys. Commun.*, 10, 343
- 766 Kargaltsev, O., Pavlov, G. G., & Wong, J. A. 2009, *The Astrophysical Journal*, 690, 891

- 767 Katagiri, H., et al. 2011, ArXiv e-prints
- 768 Kerr, M. 2011, PhD in physics, University of Washington
- 769 King, I. 1962, *AJ*, 67, 471
- 770 Krause, J., Carmona, E., & Reichardt, I. 2011, in (Presented at the 2011 Fermi Symposium,
771 Rome Italy)
- 772 Landi, R., de Rosa, A., Dean, A. J., Bassani, L., Ubertini, P., & Bird, A. J. 2007a, *MNRAS*,
773 380, 926
- 774 Landi, R., Masetti, N., Bassani, L., Cellone, S. A., Romero, G. E., Ubertini, P., & Dean,
775 A. J. 2007b, *The Astronomer’s Telegram*, 1047, 1
- 776 Landi, R., et al. 2006, *ApJ*, 651, 190
- 777 Malizia, A., et al. 2005, *ApJ*, 630, L157
- 778 Markwardt, C. B., & Ogelman, H. 1995, *Nature*, 375, 40
- 779 Matsumoto, H., et al. 2007, *PASJ*, 59, 199
- 780 —. 2008, *PASJ*, 60, 163
- 781 Mattox, J. R., et al. 1996, *ApJ*, 461, 396
- 782 Mizukami, T., et al. 2011, ArXiv e-prints
- 783 Murphy, T., Mauch, T., Green, A., Hunstead, R. W., Piestrzynska, B., Kels, A. P., &
784 Sztajer, P. 2007, *MNRAS*, 382, 382
- 785 Paron, S., Dubner, G., Reynoso, E., & Rubio, M. 2008, *A&A*, 480, 439
- 786 Petre, R., Becker, C. M., & Winkler, P. F. 1996, *ApJ*, 465, L43+
- 787 Pollock, A. M. T. 1985, *A&A*, 150, 339
- 788 Protassov, R., van Dyk, D. A., Connors, A., Kashyap, V. L., & Siemiginowska, A. 2002,
789 *ApJ*, 571, 545
- 790 Reynoso, E. M., Dubner, G. M., Goss, W. M., & Arnal, E. M. 1995, *AJ*, 110, 318
- 791 Reynoso, E. M., Green, A. J., Johnston, S., Dubner, G. M., Giacani, E. B., & Goss, W. M.
792 2003, *MNRAS*, 345, 671

- 793 Rodriguez, J., Tomsick, J. A., Foschini, L., Walter, R., Goldwurm, A., Corbel, S., & Kaaret,
794 P. 2003, *A&A*, 407, L41
- 795 Rowell, G., Horns, D., Fukui, Y., & Moriguchi, Y. 2008, in *American Institute of Physics*
796 *Conference Series*, Vol. 1085, *American Institute of Physics Conference Series*, ed.
797 F. A. Aharonian, W. Hofmann, & F. Rieger, 241–244
- 798 Sreekumar, P., et al. 1998, *The Astrophysical Journal*, 494, 523
- 799 Sugizaki, M., Mitsuda, K., Kaneda, H., Matsuzaki, K., Yamauchi, S., & Koyama, K. 2001,
800 *ApJS*, 134, 77
- 801 Swanenburg, B. N., et al. 1981, *ApJ*, 243, L69
- 802 Taylor, A. R., et al. 2003, *AJ*, 125, 3145
- 803 The Fermi-LAT Collaboration. 2010, *ArXiv e-prints*
- 804 Tomsick, J. A., Lingenfelter, R., Walter, R., Rodriguez, J., Goldwurm, A., Corbel, S., &
805 Kaaret, P. 2003, *IAU Circ.*, 8076, 1
- 806 Torii, K., et al. 1998, *ApJ*, 494, L207+
- 807 Weekes, T. C., et al. 1989, *ApJ*, 342, 379
- 808 Weinstein, A. 2009, *ArXiv e-prints*
- 809 Young, E. T., Lada, C. J., & Wilking, B. A. 1986, *ApJ*, 304, L45

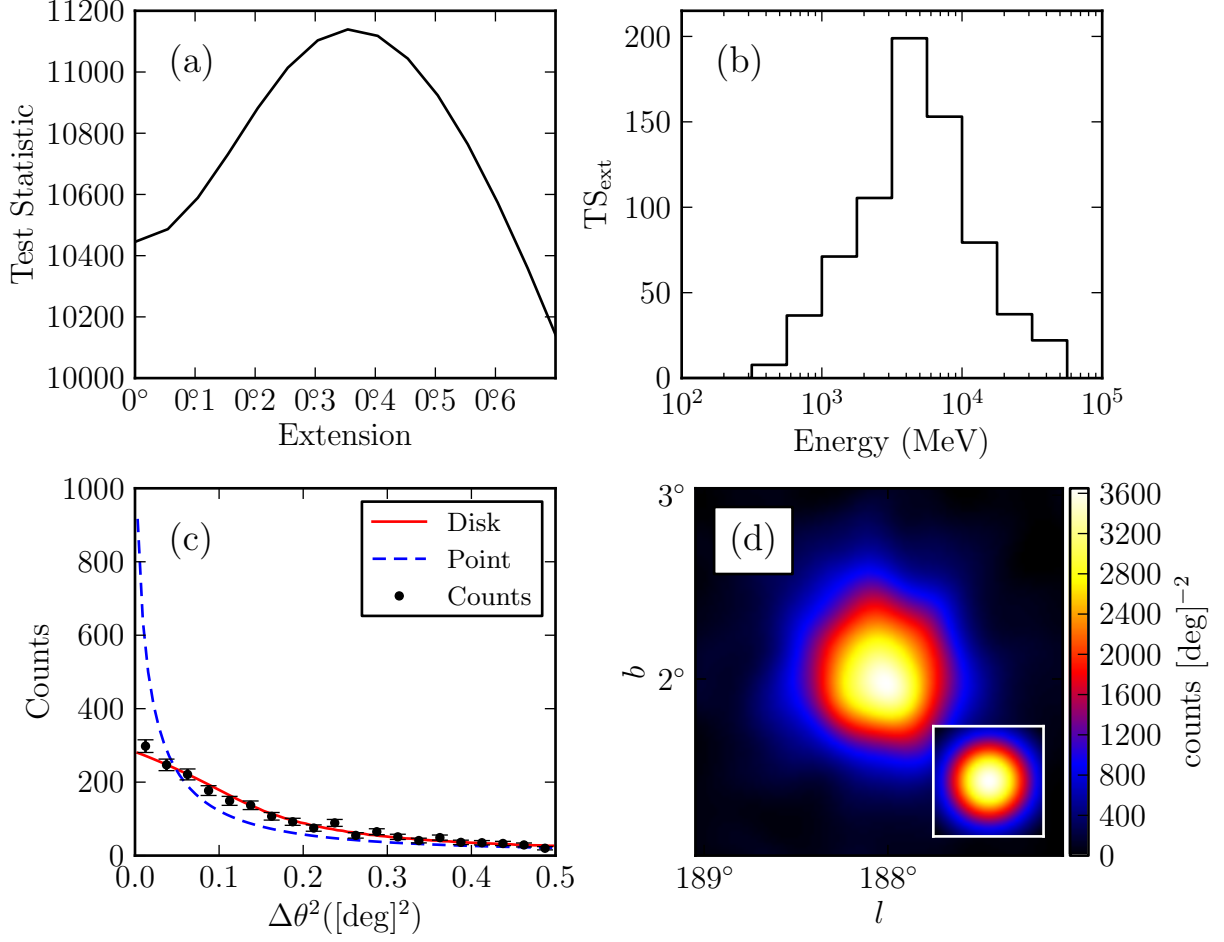


Fig. 1.— Counts maps and test statistic profiles for the SNR IC443. (a) TS vs. extension of the source. (b) TS_{ext} for individual energy bands. (c) observed radial profile of counts in comparison to the expected profiles for a spatially extended source (solid and colored red in the online version) and for a point source (dashed and colored blue in the online version). (d) smoothed count map after subtraction of the diffuse emission compared to the smoothed LAT PSF (inset). Plots (a), (c), and (d) use only 1 GeV to 100 GeV photons. Plots (c) and (d) use only photons which converted in the front part of the tracker and have an improved angular resolution.

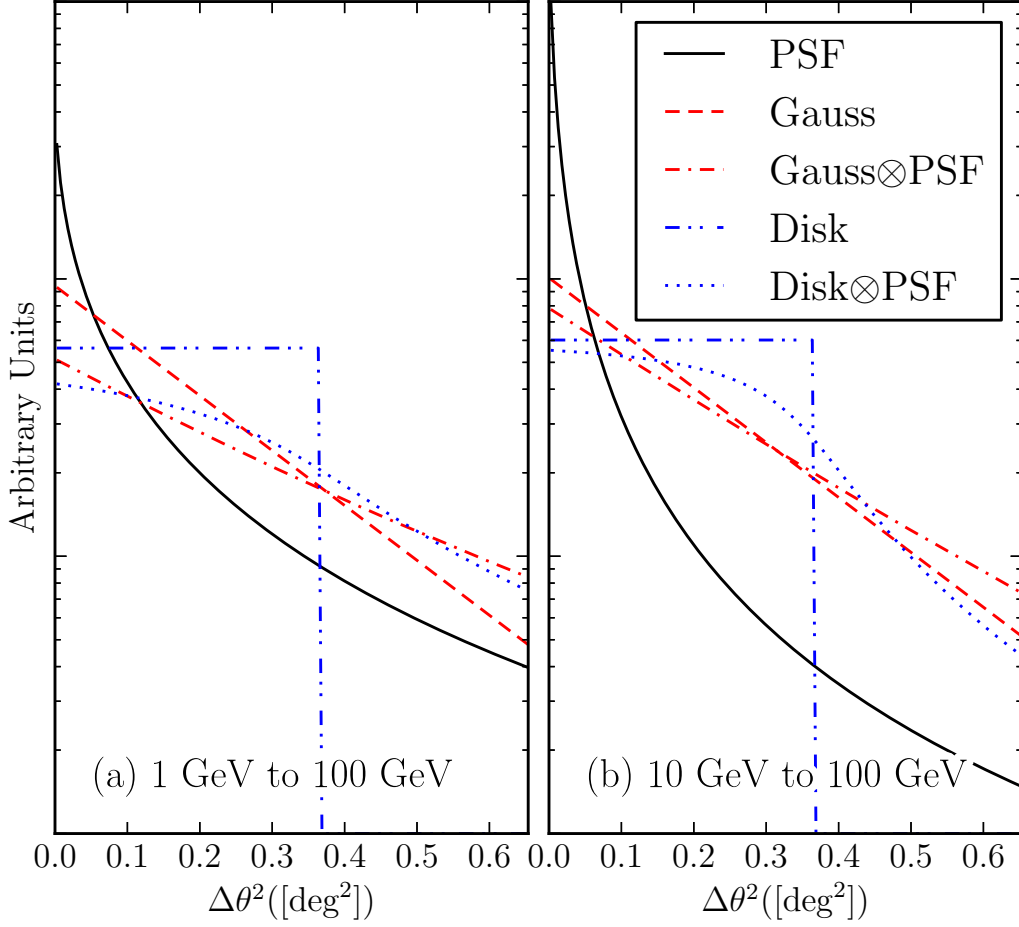


Fig. 2.— A comparison of a 2D Gaussian and disk-like surface brightness profiles of extended sources before and after convolving with the PSF for two energy ranges. The solid black line is the PSF that would be observed for a power-law source of spectral index 2. The dashed line and the dash-dotted line are the brightness profile of a Gaussian with $r_{68} = 0.5$ and the convolution of this profile with the LAT PSF respectively (colored red in the online version). The dash-dot-dotted and the dot-dotted line are the brightness profile of a uniform disk with $r_{68} = 0.5$ and the convolution of this profile with the LAT PSF respectively (colored blue in the online version).

Table 1. Monte Carlo Validation Parameters

Spectral Index	Flux ^(a) (ph cm ⁻² s ⁻¹)	N_{sims}	$\langle \text{TS} \rangle$
1.5	10^{-6}	31952	92862
	3×10^{-7}	31962	22169
	10^{-7}	31977	5806
	3×10^{-8}	31991	1270
	10^{-8}	31940	301
	3×10^{-9}	30324	62
2	10^{-6}	31872	22067
	3×10^{-7}	31890	4898
	10^{-7}	31858	1097
	3×10^{-8}	31632	236
	10^{-8}	27491	103
2.5	10^{-6}	31822	4706
	3×10^{-7}	31822	889
	10^{-7}	31169	176
	3×10^{-8}	21591	41
3	10^{-6}	31763	929
	3×10^{-7}	31665	161
	10^{-7}	19271	40

^(a)Integral 1 GeV to 100 GeV flux.

Note. — A list of the spectral models of the simulated point sources which were tested for extension. For each model, the number of statistically independent simulations and the average value of TS is also tabulated. The models spans representative spectral parameters.

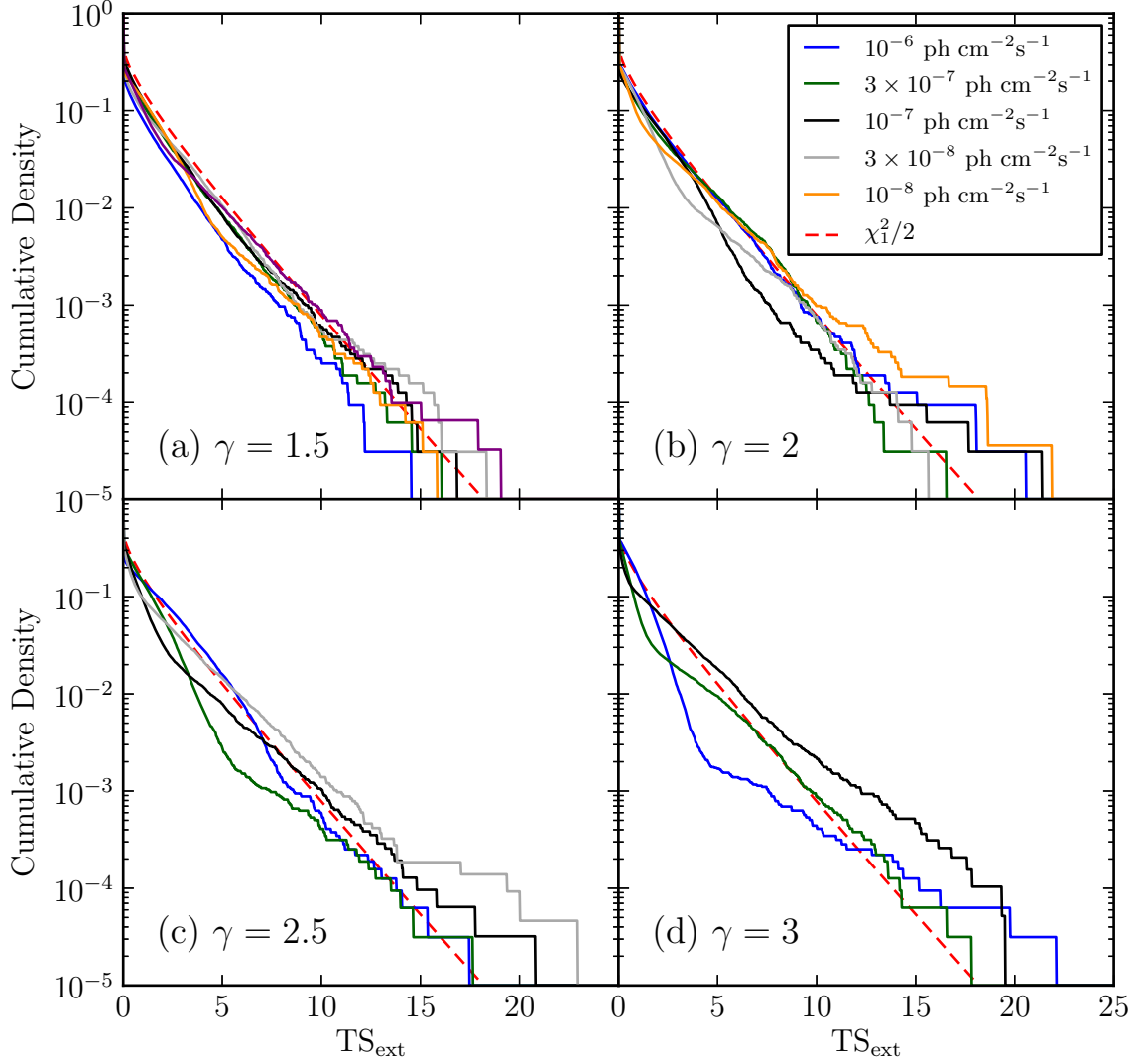


Fig. 3.— Distribution of the test statistic for the extension test. The four plots represent simulated point sources of different spectral indices and the different lines (colored in the online version) represent point sources with different 100 MeV to 100 GeV integral fluxes. The dashed line (colored red) is the cumulative density function of Equation 9.

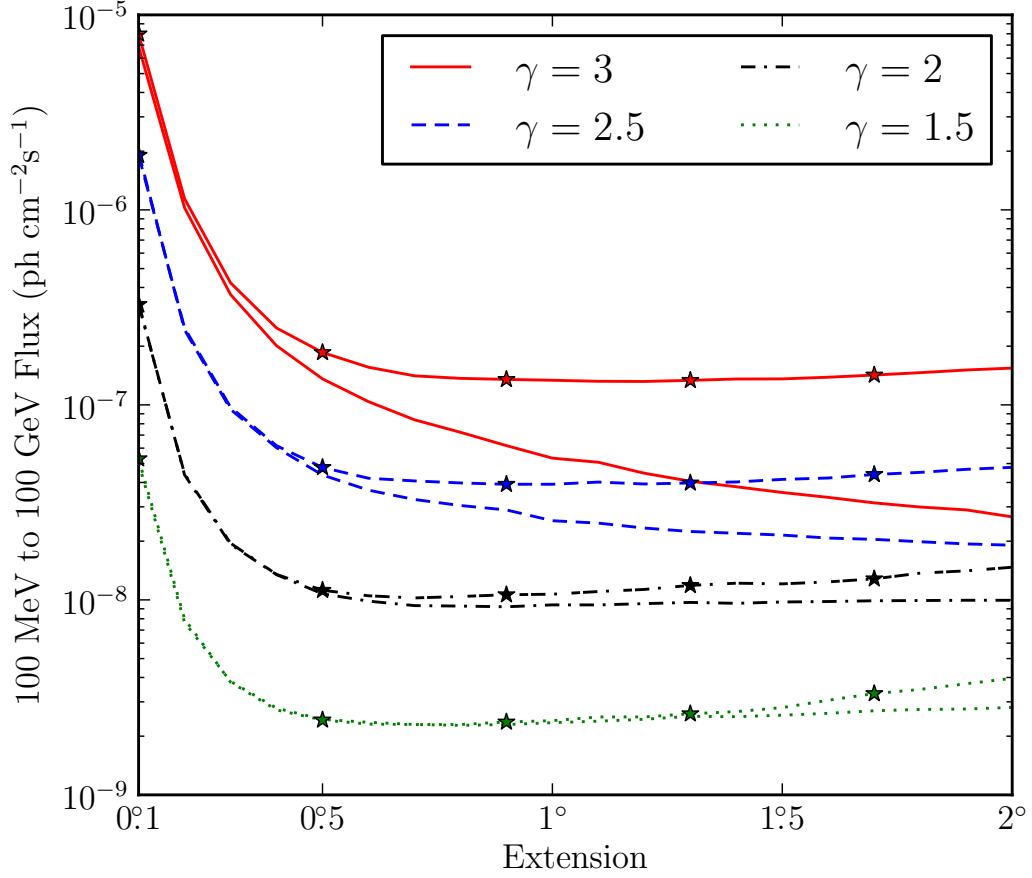


Fig. 4.— The detection threshold to resolve a uniform disk extended source for a two-year exposure. All sources have an assumed power-law spectrum and the different colors correspond to different simulated spectral indices. The solid line is the detection threshold using photons with energies between 100 MeV and 100 GeV while the dashed line is the threshold using 1 GeV to 100 GeV photons.

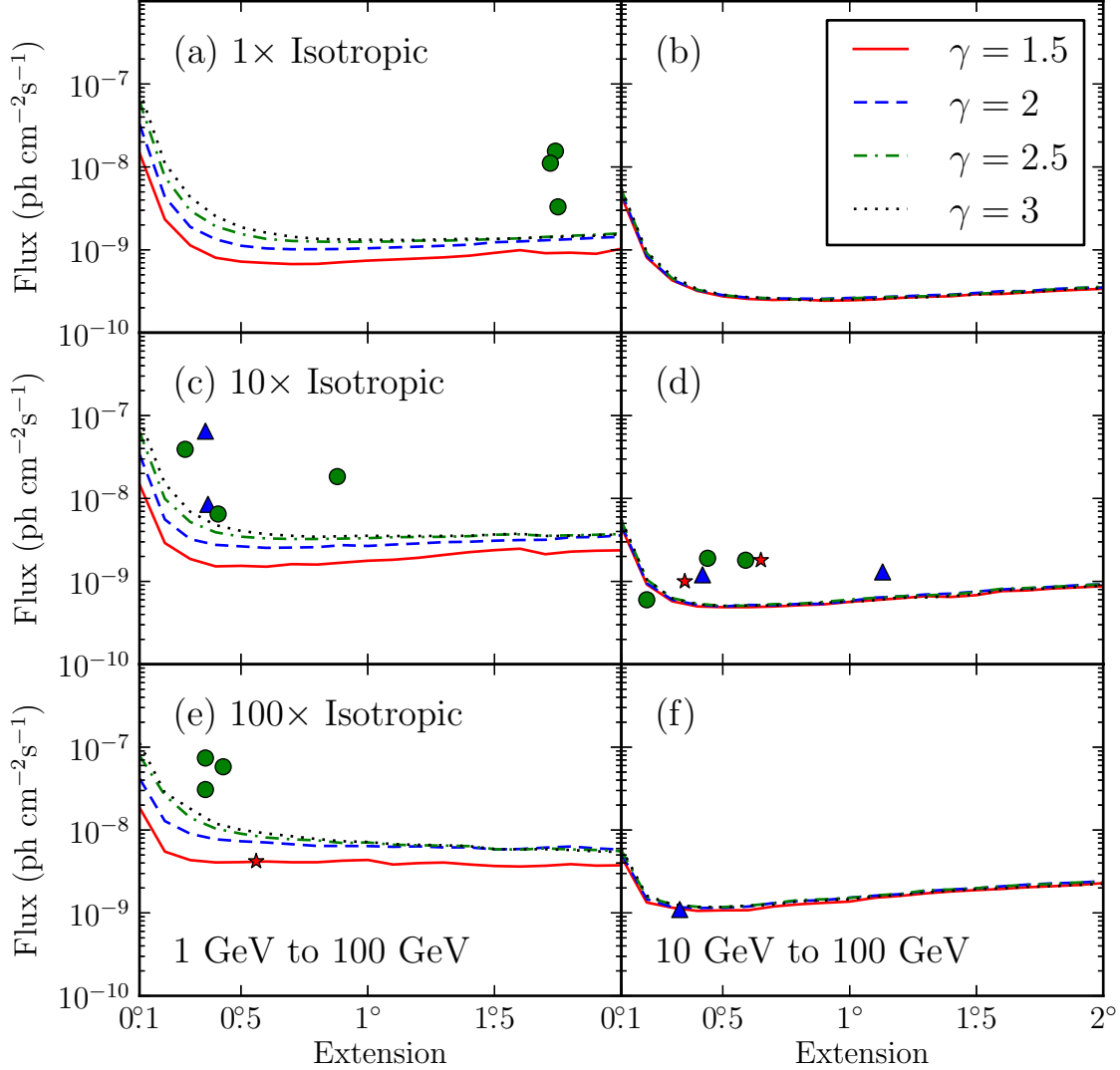


Fig. 5.— the LAT detection threshold for four spectral indices and three background ($1\times$, $10\times$, and $100\times$ the Sreekumar-like isotropic spectrum) for a two-year exposure. The left plots are the detection threshold when using 1 GeV to 100 GeV photons and the right plots are the detection threshold when using 10 GeV to 100 GeV photons. The flux is integrated only in the selected energy range. Overlaid on this plot are the LAT detected extended sources placed by the magnitude of the nearby Galactic diffuse emission and the energy range they were analyzed with. The star shaped markers (colored red in the electronic version) are sources with a spectral index closer to 1.5, the triangular markers (colored blue) an index closer to 2, and the circular markers (colored green) an index closer to 2.5. The circular marker in plot (d) below the sensitivity line is MSH 15–52.

Table 2. Extension Detection Threshold

γ	BG	0.1	0.2	0.3	0.4	0.5	0.6	0.7	0.8	0.9	1.0	1.1	1.2	1.3	1.4	1.5	1.6	1.7	1.8	1.9	2.0
E>1 GeV																					
1.5	1×	148.1	23.3	11.3	8.0	7.2	6.9	6.7	6.8	7.1	7.4	7.6	7.9	8.1	8.5	9.2	9.9	9.1	9.2	9.0	10.3
	10×	148.4	29.0	18.7	15.2	15.4	15.0	16.1	16.0	16.8	17.7	18.2	19.3	20.9	22.5	23.8	24.8	21.3	22.8	23.4	23.7
	100×	186.8	55.0	43.4	40.7	41.0	41.8	40.9	40.9	42.7	43.6	38.4	39.9	40.6	38.4	36.9	36.3	37.1	38.8	37.2	37.6
2	1×	328.4	43.4	18.9	13.4	11.2	10.4	10.2	10.2	10.2	10.4	10.7	10.9	11.2	11.5	12.4	12.6	13.0	13.4	14.0	14.4
	10×	341.0	55.9	32.3	27.6	26.5	25.4	25.6	25.9	27.4	26.8	27.8	28.7	29.8	30.1	31.0	31.5	31.7	34.0	34.3	35.9
	100×	420.5	128.3	90.2	77.3	73.3	70.8	67.5	64.3	64.2	64.1	62.8	63.6	61.7	61.9	58.4	59.0	61.4	63.3	60.1	58.1
2.5	1×	627.1	75.6	29.8	19.3	15.5	13.5	12.8	12.6	12.5	12.5	12.6	12.9	12.9	13.1	13.5	13.7	14.3	14.8	15.2	15.8
	10×	638.9	99.1	52.1	39.1	34.6	33.0	32.5	32.5	32.8	33.2	34.1	34.3	34.5	35.1	36.6	36.9	35.5	36.0	36.5	37.3
	100×	795.0	262.1	140.9	104.3	90.4	81.2	77.2	75.1	69.7	70.9	66.5	65.6	64.9	64.0	58.9	58.1	60.2	58.4	57.5	55.8
3	1×	841.5	110.6	43.2	25.5	18.7	16.1	14.4	13.6	13.3	13.2	13.1	13.1	13.4	13.6	13.5	13.8	14.2	14.4	14.8	15.4
	10×	921.6	151.3	69.1	47.8	40.7	37.1	35.5	34.5	35.1	35.5	35.3	35.3	35.4	35.5	36.8	37.6	35.3	35.4	36.3	36.6
	100×	1124.1	282.9	181.1	119.8	100.7	91.1	84.3	77.9	73.3	71.8	67.6	66.4	65.5	63.9	59.0	58.6	58.8	57.5	55.4	54.4
E>10 GeV																					
1.5	1×	44.6	8.0	4.3	3.2	2.7	2.6	2.5	2.5	2.4	2.5	2.5	2.6	2.7	2.8	2.9	2.9	3.1	3.2	3.3	3.4
	10×	45.2	9.2	5.8	5.0	4.9	4.9	5.0	5.2	5.3	5.7	5.9	6.3	6.6	6.5	6.8	7.6	7.8	8.2	8.5	8.7
	100×	47.3	13.4	11.6	10.6	10.8	10.8	12.0	12.7	13.2	13.7	15.3	16.1	17.2	18.2	18.9	19.5	20.4	21.0	21.7	22.9
2	1×	49.7	8.4	4.4	3.3	2.8	2.6	2.6	2.6	2.6	2.6	2.7	2.7	2.8	2.9	3.0	3.2	3.2	3.4	3.5	3.5
	10×	48.6	9.5	6.0	5.2	5.0	5.2	5.2	5.3	5.4	5.8	6.4	6.6	7.0	7.1	7.5	8.0	8.3	8.6	9.0	9.2
	100×	51.8	14.7	11.8	11.5	11.5	11.9	13.2	14.0	14.3	15.3	16.2	16.9	18.4	19.2	19.8	21.0	22.0	22.8	23.2	24.3
2.5	1×	53.1	9.1	4.5	3.3	2.8	2.7	2.6	2.5	2.5	2.6	2.7	2.7	2.8	2.8	2.9	3.1	3.2	3.3	3.5	3.6
	10×	53.7	10.5	6.3	5.4	5.1	5.1	5.3	5.4	5.7	6.0	6.3	6.6	6.8	6.9	7.5	8.1	8.3	8.6	8.9	9.2
	100×	57.0	15.6	12.7	11.9	11.8	12.2	13.1	14.3	14.6	15.2	16.3	17.0	18.8	19.2	19.9	21.0	21.9	22.3	23.3	23.7
3	1×	55.5	9.4	4.8	3.4	2.9	2.7	2.6	2.5	2.5	2.5	2.6	2.7	2.7	2.8	2.9	3.0	3.1	3.2	3.4	3.4
	10×	56.0	10.5	6.2	5.3	5.1	5.1	5.1	5.3	5.5	5.7	5.9	6.4	6.4	6.6	7.0	7.8	8.0	8.3	8.6	8.9
	100×	60.3	16.2	12.7	11.7	11.8	12.2	12.6	13.8	14.2	14.6	15.8	16.5	17.6	18.5	19.4	19.8	20.7	21.0	21.8	22.5

Note. — The detection threshold to resolve a uniform disk spatially extended sources for a two-year exposure for sources of varying energy ranges, spectral indices, and background levels. The extended sources were simulated against a Sreekumar-like isotropic spectrum and the second column is the factor that the simulated background was scaled by. The remaining columns are varying sizes of the source. The table quotes integral fluxes in the analyzed energy range (1 GeV to 100 GeV or 10 GeV 100 GeV) in units of 10^{-10} ph cm $^{-2}$ s $^{-1}$.

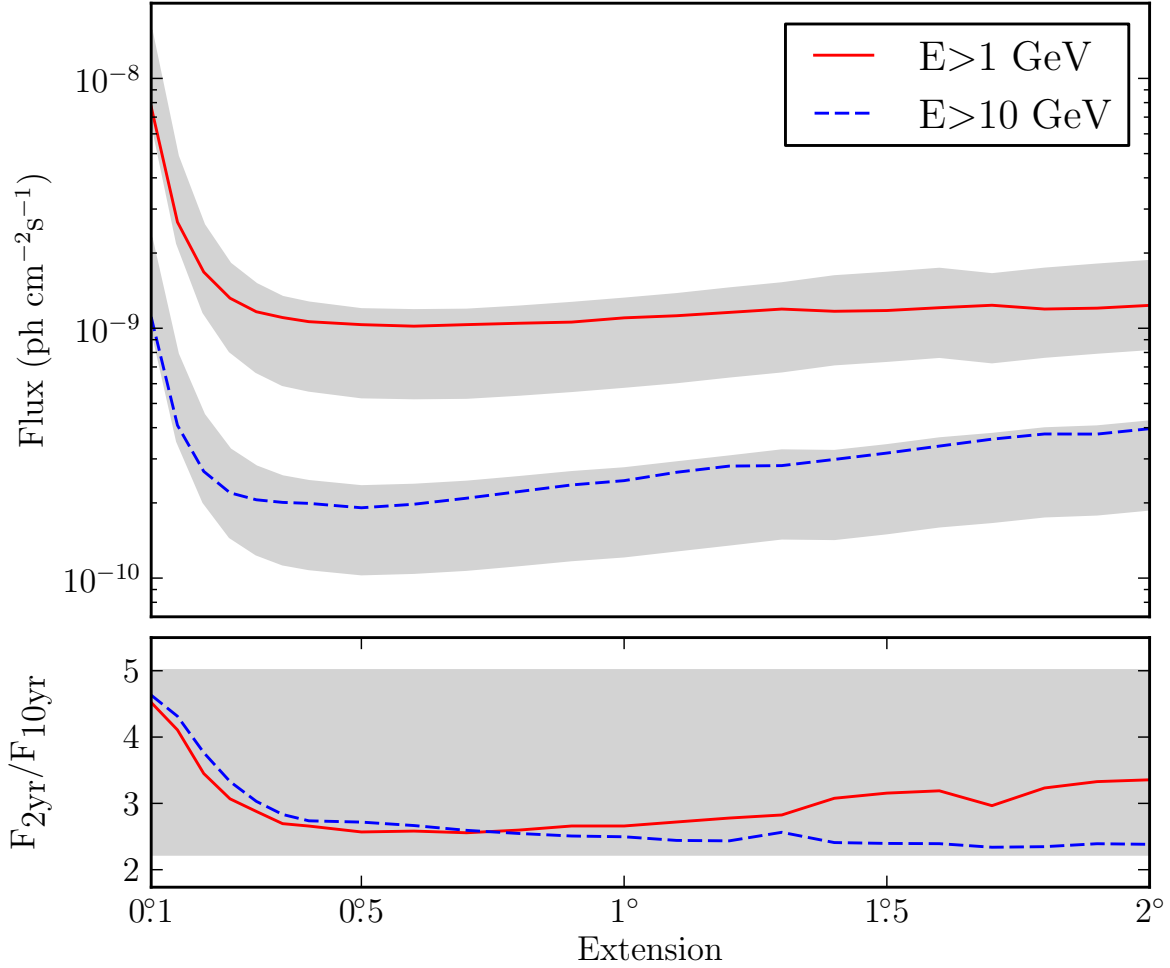


Fig. 6.— The LAT’s projected detection threshold to extension after a ten-year exposure for a power-law source of spectral index 2 against 10 times the isotropic background in the energy range from 1 GeV to 100 GeV (solid line colored red in the electronic version) and 10 GeV to 100 GeV (dashed line colored blue). The solid gray regions represent the detection threshold assuming the sensitivity improves from 2 to 10 years by the square root of the exposure (top edge) and linearly with exposure (bottom edge). The lower plot shows the factor increase in sensitivity. For small extended sources, our detection threshold to the extension of a source will improve by a factor larger than the square root of the exposure.

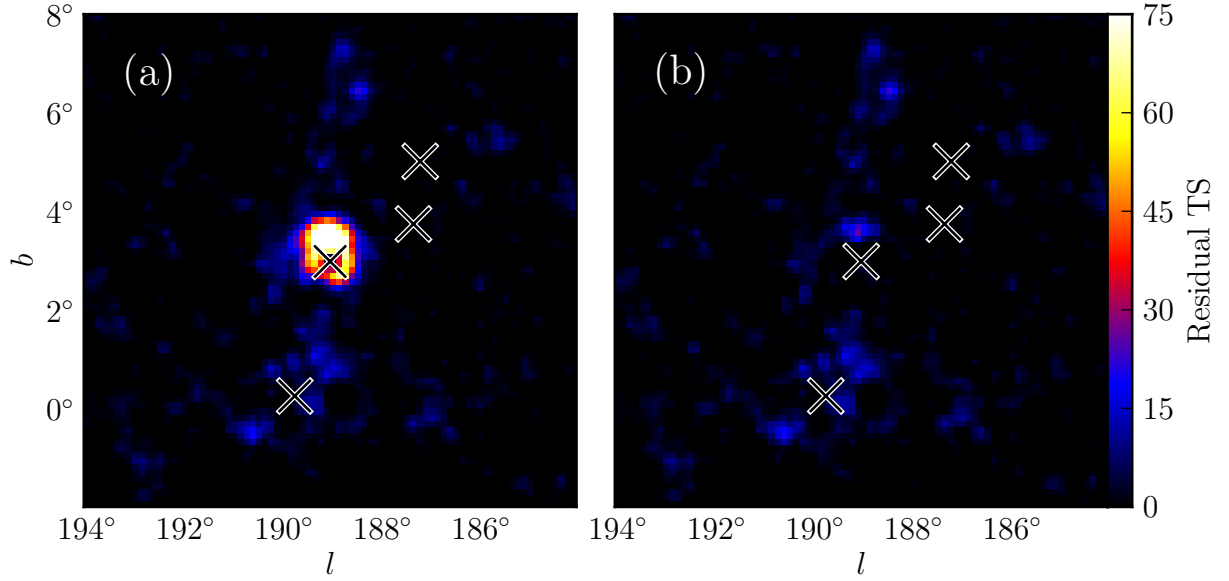


Fig. 7.— A test statistic map generated for the region around the SNR IC443 using 1 GeV to 100 GeV photons. (a) test statistic map after subtracting IC443 modeled as a point source. (b) same as (a), but IC443 modeled as extended source. Crosses represent sources included in the model of the region.

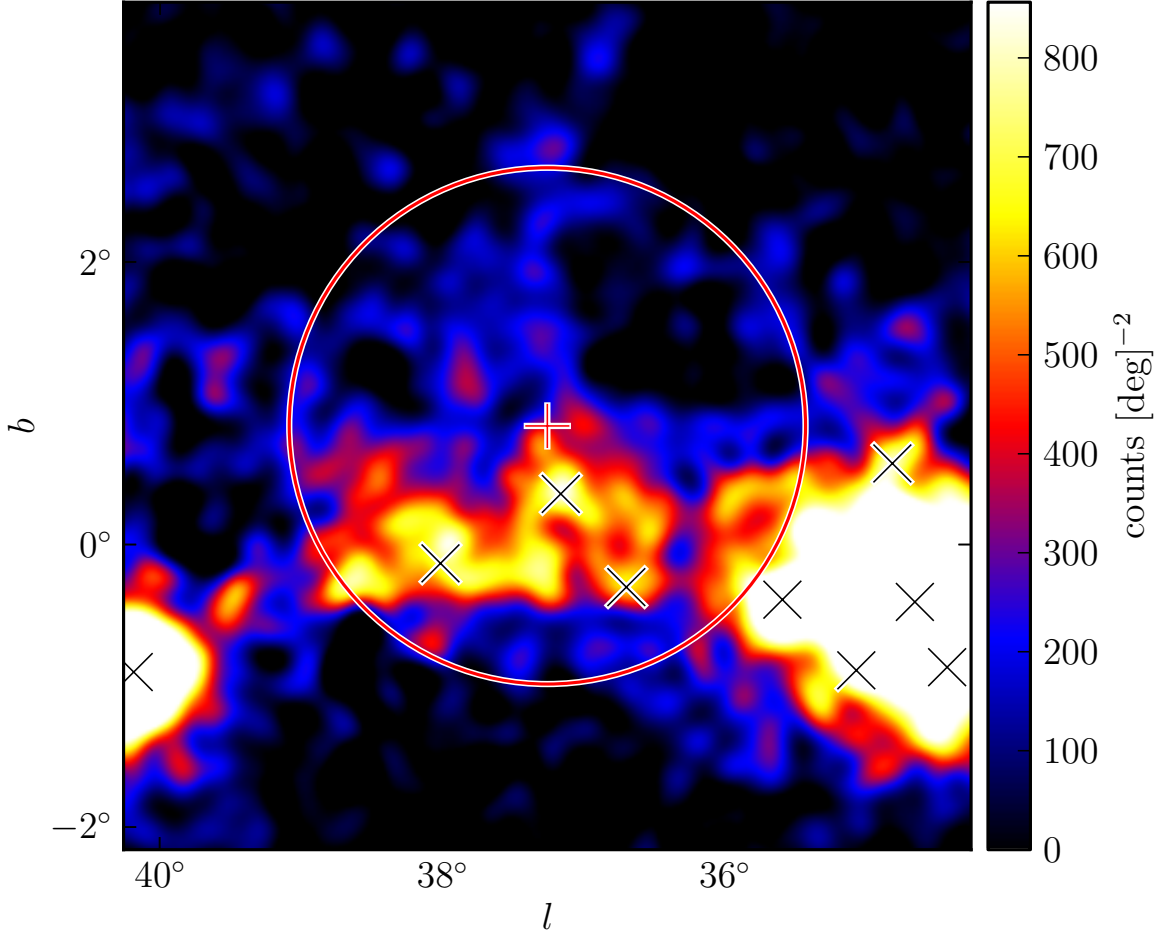


Fig. 8.— A diffuse-emission-subtracted 1 GeV to 100 GeV counts map of the region around 2FGL J1856.2+0450c smoothed by a 0.1° 2D Gaussian kernel. The plus-shaped marker and circle (colored red in the online version) represent the center and size of the best fit radially symmetric source with a uniform intensity profile. The black crosses represent the position of other 2FGL sources. The extension is statistically significant, but the extension encompasses many 2FGL sources and the emission does not look to be uniform. This source is probably fitting large-scale diffuse residual features. Although the fit is statistically significant, it likely corresponds to residual features of inaccurately modeled diffuse emission picked up by the fit. We manually discard candidates that appear like this.

Table 3. Analysis of the twelve extended sources included in 2FGL

Name	GLON (deg.)	GLAT (deg.)	σ (deg.)	TS	TS _{ext}	Pos Err (deg.)	Flux ^(a) (ph cm ⁻² s ⁻¹)	Index
E>1 GeV								
SMC	302.68	-44.81	$1.75 \pm 0.07 \pm 0.02$	94.8	67.4	0.12	3.3 ± 0.4	2.41 ± 0.17
LMC	279.10	-32.61	$1.74 \pm 0.05 \pm 0.13$	1101.3	860.5	0.05	15.5 ± 0.6	2.48 ± 0.06
IC443	189.05	3.04	$0.36 \pm 0.01 \pm 0.04$	10719.8	510.4	0.01	64.8 ± 1.2	2.23 ± 0.02
Vela X	263.34	-3.11	0.88					
Centarus A	309.52	19.42	~ 10					
W28	6.50	-0.27	$0.43 \pm 0.02 \pm 0.03$	1324.8	177.4	0.01	58.0 ± 1.8	2.63 ± 0.03
W30	8.61	-0.20	$0.36 \pm 0.02 \pm 0.02$	465.4	73.3	0.02	30.7 ± 1.6	2.59 ± 0.04
W44	34.69	-0.38	$0.36 \pm 0.01 \pm 0.02$	1903.3	217.7	0.01	73.6 ± 1.8	2.68 ± 0.02
W51C	49.13	-0.45	$0.28 \pm 0.02 \pm 0.05$	1819.5	115.7	0.01	39.3 ± 1.3	2.35 ± 0.03
Cygnus Loop	74.22	-8.46	$1.72 \pm 0.05 \pm 0.07$	356.5	356.5	0.06	11.1 ± 0.7	2.53 ± 0.11
E>10 GeV								
MSH 15–52	320.38	-1.22	$0.20 \pm 0.04 \pm 0.03$	76.2	6.5	0.03	0.6 ± 0.7	2.27 ± 0.73
HESS J1825–137	17.56	-0.46	$0.65 \pm 0.03 \pm 0.01$	83.6	55.9	0.05	1.8 ± 0.2	1.74 ± 0.19

^(a)Integrated in the fit energy range (either 1 GeV 100 GeV or 10 GeV 100 GeV).

Note. — All sources were fit using a spatial model assuming a uniform radially symmetric intensity distribution. GLON and GLAT are Galactic longitude and latitude of the best fit extended source respectively. The first error on σ is statistical and the second is systematic (see Section 5.2). Pos Err is the error on the position of the source. Vela X and the Centarus A Lobes were not fit in our analysis but are include for completeness.

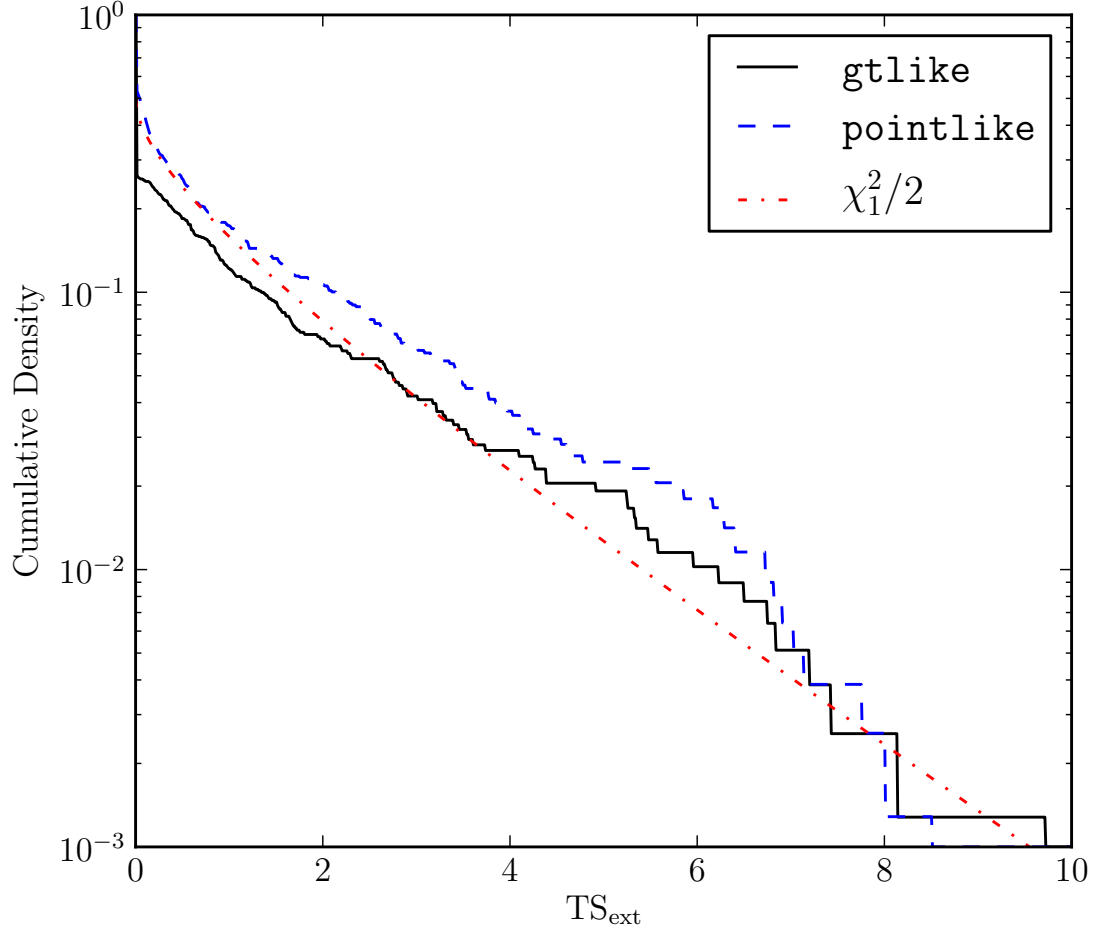


Fig. 9.— The cumulative density of TS_{ext} for 783 of the clean AGN in 2LAC which are significant above 1 GeV calculated with `pointlike` (dashed line colored blue in the electronic version) and with `gtlike` (solid line colored red). AGN are too far and too small to be resolved by the LAT. Therefore, the cumulative density of TS_{ext} is expected to follow a $\chi^2/2$ distribution (Equation 9, the dash-dotted line colored red).

Table 4. Extension fit for the nine new extended sources

Name	GLON (deg.)	GLAT (deg.)	σ (deg.)	TS	TS _{ext}	Pos Err (deg.)	Flux ^(a) (ph cm ⁻² s ⁻¹)	Index	Counterpart
E>1 GeV									
2FGL J0823.0–4246	260.32	-3.28	$0.37 \pm 0.03 \pm 0.02$	320.9	46.3	0.02	8.5 ± 0.7	2.20 ± 0.09	Puppis A
2FGL J1627.0–2425c	353.08	16.78	$0.41 \pm 0.05 \pm 0.02$	144.5	31.1	0.04	6.5 ± 0.6	2.49 ± 0.14	Ophiuchus
2FGL J1712.4–3941	347.25	-0.54	$0.56 \pm 0.04 \pm 0.01$	75.0	39.6	0.05	4.2 ± 0.9	1.47 ± 0.12	RX J1713.7–3946
E>10 GeV									
2FGL J0851.7–4635	266.29	-1.43	$1.13 \pm 0.08 \pm 0.05$	116.1	87.2	0.07	1.3 ± 0.2	1.76 ± 0.21	Vela Jr.
2FGL J1615.0–5051	332.38	-0.14	$0.33 \pm 0.04 \pm 0.01$	53.4	16.3	0.04	1.1 ± 0.2	2.24 ± 0.28	HESS J1616–508
2FGL J1615.2–5138	331.66	-0.66	$0.42 \pm 0.03 \pm 0.01$	76.6	48.0	0.05	1.2 ± 0.2	1.77 ± 0.24	HESS J1614–518
2FGL J1632.4–4753c	336.41	0.22	$0.44 \pm 0.04 \pm 0.03$	127.8	64.5	0.04	1.9 ± 0.2	2.29 ± 0.21	HESS J1632–478
2FGL J1837.3–0700c	25.08	0.13	$0.35 \pm 0.08 \pm 0.03$	46.2	18.8	0.07	1.0 ± 0.2	1.63 ± 0.29	HESS J1837–069
2FGL J2021.5+4026	78.18	2.19	$0.59 \pm 0.03 \pm 0.02$	222.2	116.4	0.04	1.8 ± 0.2	2.31 ± 0.19	γ -Cygni

^(a)Integrated in the fit energy range (either 1 GeV to 100 GeV or 10 GeV 100 GeV).

Note. — The columns in this table have the same meaning as those in Table 3.

Table 5. Dual localization, alternative PSF, and alternative diffuse results

Name	TS _{pointlike}	TS _{gtlike}	TS _{alt,diff}	TS _{extpointlike}	TS _{extgtlike}	TS _{extalt,diff}	σ (deg.)	$\sigma_{\text{alt,diff}}$ (deg.)	$\sigma_{\text{alt,psf}}$ (deg.)	TS _{inc}
E>1 GeV										
2FGL J0823.0–4246	350.9	320.9	352.5	66.0	46.3	53.6	0.37	0.39	0.38	22.1
2FGL J1627.0–2425c	170.2	144.5	112.6	43.9	31.1	23.9	0.41	0.40	0.39	20.0
2FGL J1712.4–3941	80.9	75.0	43.4	47.4	39.6	22.2	0.56	0.56	0.54	6.4
E>10 GeV										
2FGL J0851.7–4635	116.7	116.1	122.3	87.1	87.2	90.4	1.13	1.16	1.17	16.1
2FGL J1615.0–5051	52.4	53.4	55.6	17.5	16.3	17.4	0.33	0.32	0.32	11.9
2FGL J1615.2–5138	76.3	76.6	86.3	44.0	48.0	52.6	0.42	0.43	0.43	37.0
2FGL J1632.4–4753c	126.6	127.8	120.7	63.9	64.5	64.1	0.44	0.44	0.47	40.6
2FGL J1837.3–0700c	45.4	46.2	39.0	18.5	18.8	16.6	0.35	0.34	0.38	12.6
2FGL J2021.5+4026	234.3	222.2	235.6	135.9	116.4	121.4	0.59	0.60	0.60	24.3

Note. — TS_{pointlike}, TS_{gtlike}, and TS_{alt,diff} are the test statistic values from `pointlike`, `gtlike`, and `gtlike` with the alternate diffuse model respectively. TS_{extpointlike}, TS_{extgtlike}, and TS_{extalt,diff} are the test statistic values of the extension test from `pointlike`, `gtlike`, and `gtlike` with the alternate diffuse model respectively. σ , $\sigma_{\text{alt,diff}}$, and $\sigma_{\text{alt,psf}}$ are the fit extension with the standard analysis, the alternate diffuse model, and the alternate PSF respectively. TS_{inc} is the test statistic for the two point source hypothesis test (see Section 2.4).

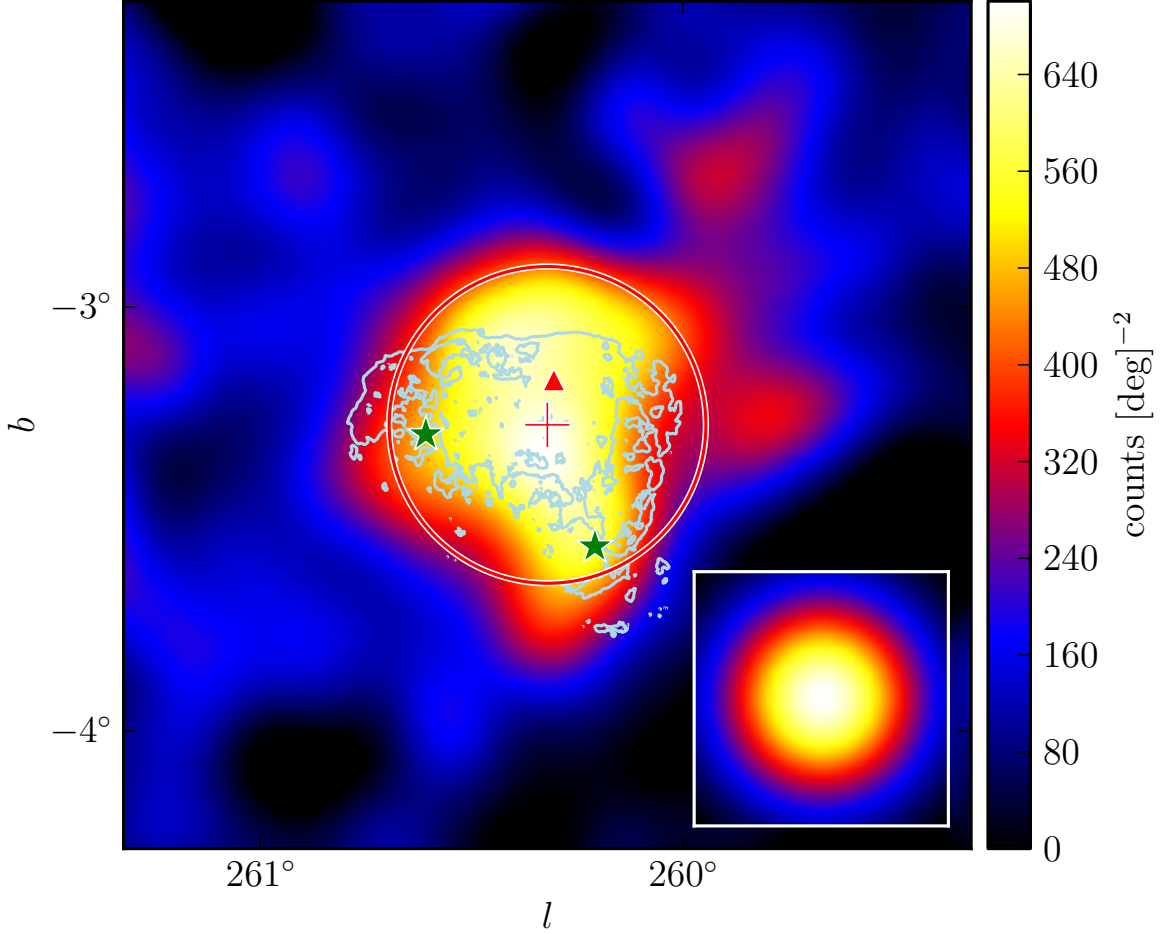


Fig. 10.— A diffuse-emission-subtracted 1 GeV to 100 GeV counts map of the region around 2FGL J0823.0–4246 smoothed by a 0.1° 2D Gaussian kernel. The triangular marker (colored red in the online version) represents the 2FGL position of this source. The plus-shaped marker and the circle (colored red) represent the best fit position and extension of this source assuming a radially symmetric uniform surface brightness. The two star-shaped markers (colored green) represent 2FGL sources that were removed from the background model. The lower right inset is the model predicted emission from a point source with the same spectrum as 2FGL J0823.4–4305 smoothed by the same kernel. This source is spatially coincident with the Puppis A SNR. The light blue contours correspond to the X-ray image of Puppis A observed by *ROSAT* (Petre et al. 1996).

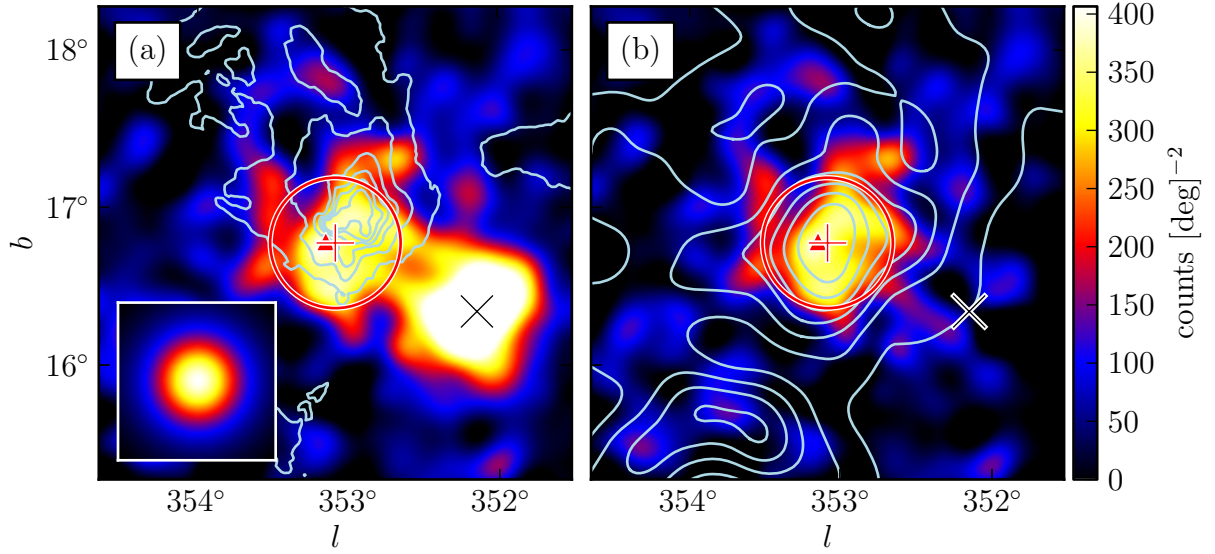


Fig. 11.— A diffuse-emission-subtracted 1 GeV to 100 GeV counts map of (a) the region around 2FGL J1627.0–2425 smoothed by a $0^\circ.1$ 2D Gaussian kernel (b) also the emission from the background source 2FGL J1625.7–2526 subtracted. The triangular marker (colored red in the online version) represents the 2FGL position of this source. The plus-shaped marker and the circle (colored red) represent the best fit position and extension of this source assuming a radially symmetric uniform surface brightness. The contours in (a) correspond to the 100 micrometer image observed by IRAS (Young et al. 1986). The contours in (b) correspond to ^{12}CO ($J = 1 \rightarrow 0$) emission integrated from -8 km/s to 20 km/s. They are from de Geus et al. (1990), were cleaned using the moment-masking technique (Dame 2011), and have been smoothed by a $0^\circ.25$ 2D Gaussian kernel.

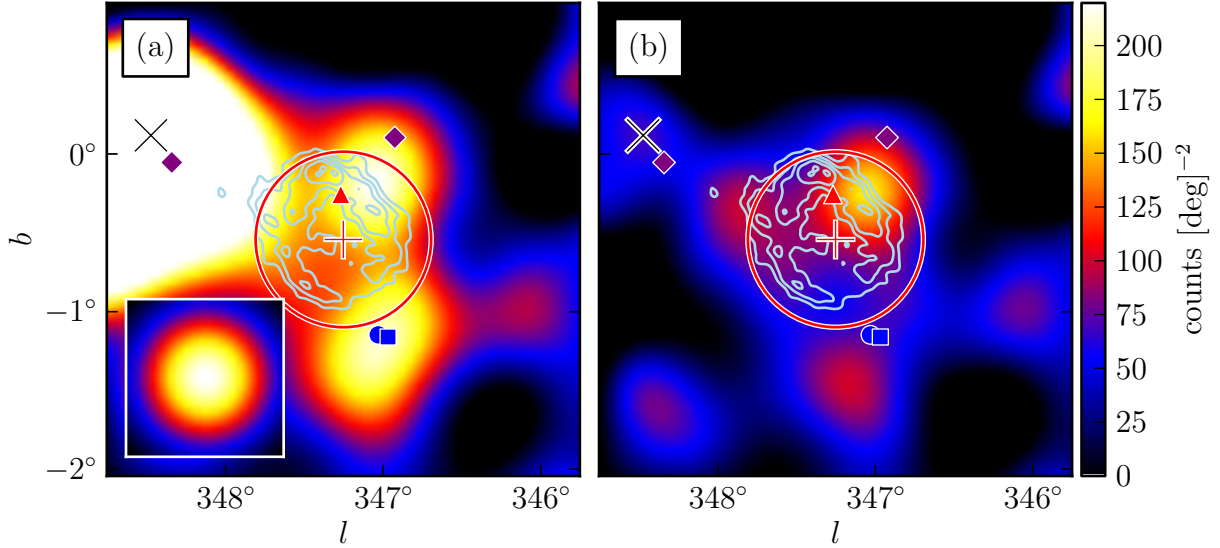


Fig. 12.— A diffuse-emission-subtracted 1 GeV to 100 GeV counts map of the region around 2FGL J1712.4–3941 (a) smoothed by a 0.25 2D Gaussian kernel and (b) with the emission from the background sources subtracted. This source is spatially coincident with RX J1713.7–3946 and was recently reported by Abdo et al. (2011c). The triangular marker (colored red in the online version) represents the 2FGL position of this source. The plus-shaped marker and the circle (colored red) are the best fit position and extension of this source assuming a radially symmetric uniform surface brightness. The contours (colored light blue) correspond to the TeV image (Aharonian et al. 2007b). The region was analyzed with the same background model as Abdo et al. (2011c). Source A is coincident with 2FGL J1715.4–4024c and the circular and square-shaped marker (colored blue) represent the 2FGL and relocalized position of this source respectively. The diamond-shaped markers (colored purple) represent the position of source B and C that were added to the background model.

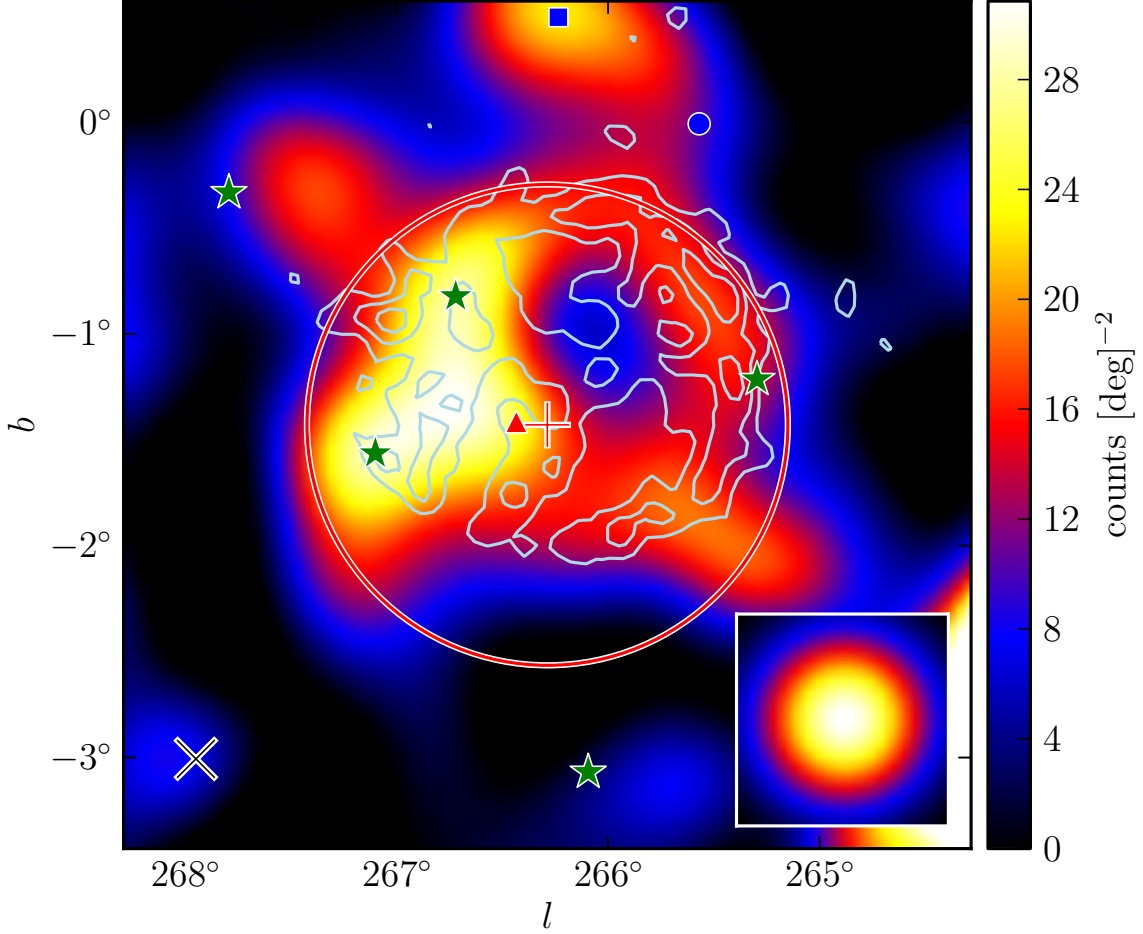


Fig. 13.— A diffuse-emission-subtracted 10 GeV to 100 GeV counts map of the region around 2FGL J0851.7–4635 smoothed by a 0.25° 2D Gaussian kernel. The triangular marker (colored red in the electronic version) represents the 2FGL position of this source. The plus-shaped marker and the circle (colored red) are the best fit position and extension of this source assuming a radially symmetric uniform surface brightness. The five star-shaped markers (colored green) represent 2FGL sources that were removed from the background model. The circular and square marker (colored blue) represents the 2FGL and relocalized position of 2FGL J0854.7–4501 respectively. This extended source is spatially coincident with the Vela Jr. SNR. The contours (colored light blue) correspond to the TeV image of Vela Jr. (Aharonian et al. 2007a).

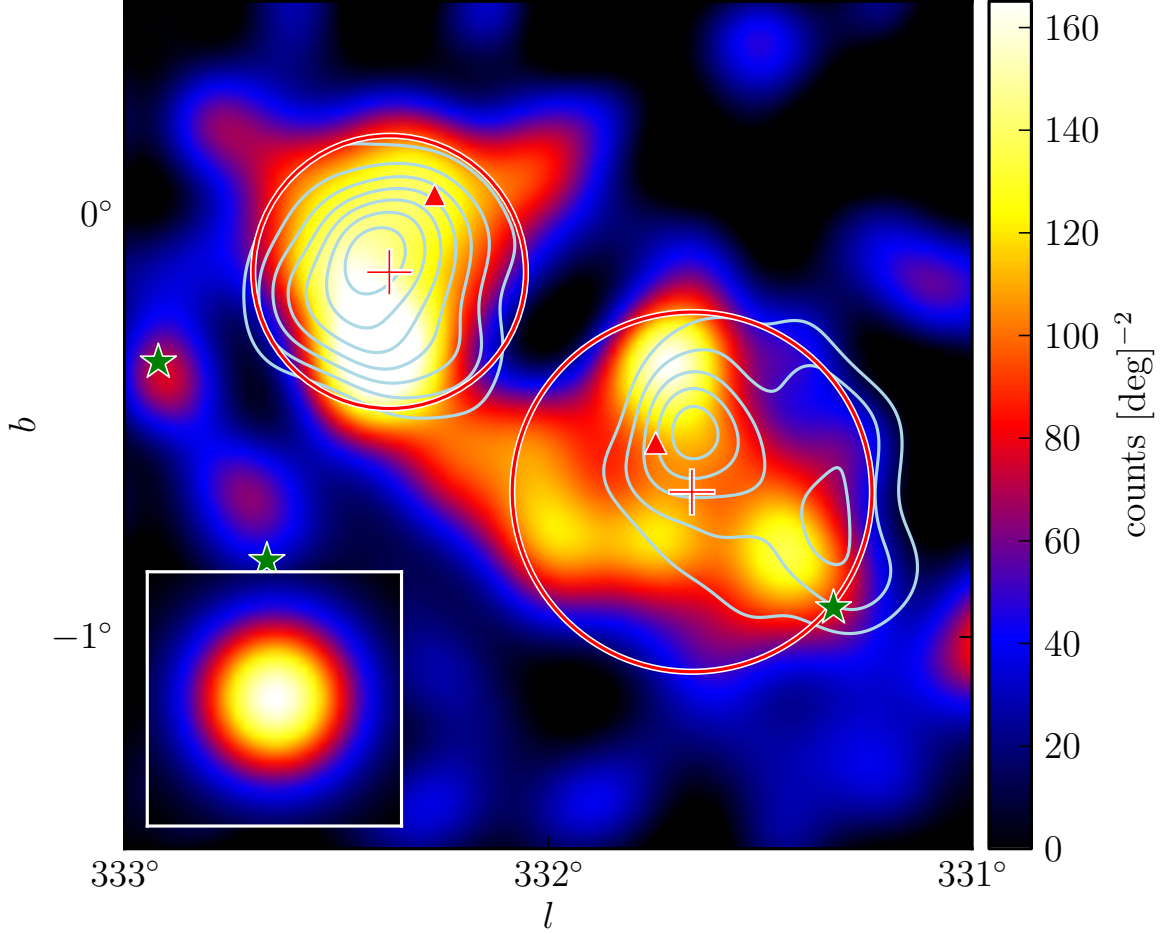


Fig. 14.— A diffuse-emission-subtracted 10 GeV to 100 GeV counts map of the region around 2FGL J1615.0–5051 (upper left) and 2FGL J1615.2–5138 (lower right) smoothed by a 0.1° 2D Gaussian kernel. The triangular markers (colored red in the electronic version) represent the 2FGL positions of these sources. The cross-shaped markers and the circles (colored red) represent the best fit positions and extensions of these sources assuming a radially symmetric uniform surface brightness. The three star-shaped markers (colored green) represent 2FGL sources that were removed from the background model. The contours (colored light blue) correspond to the TeV image of HESS J1616–508 (left) and HESS J1614–518 (right) (Aharonian et al. 2006).

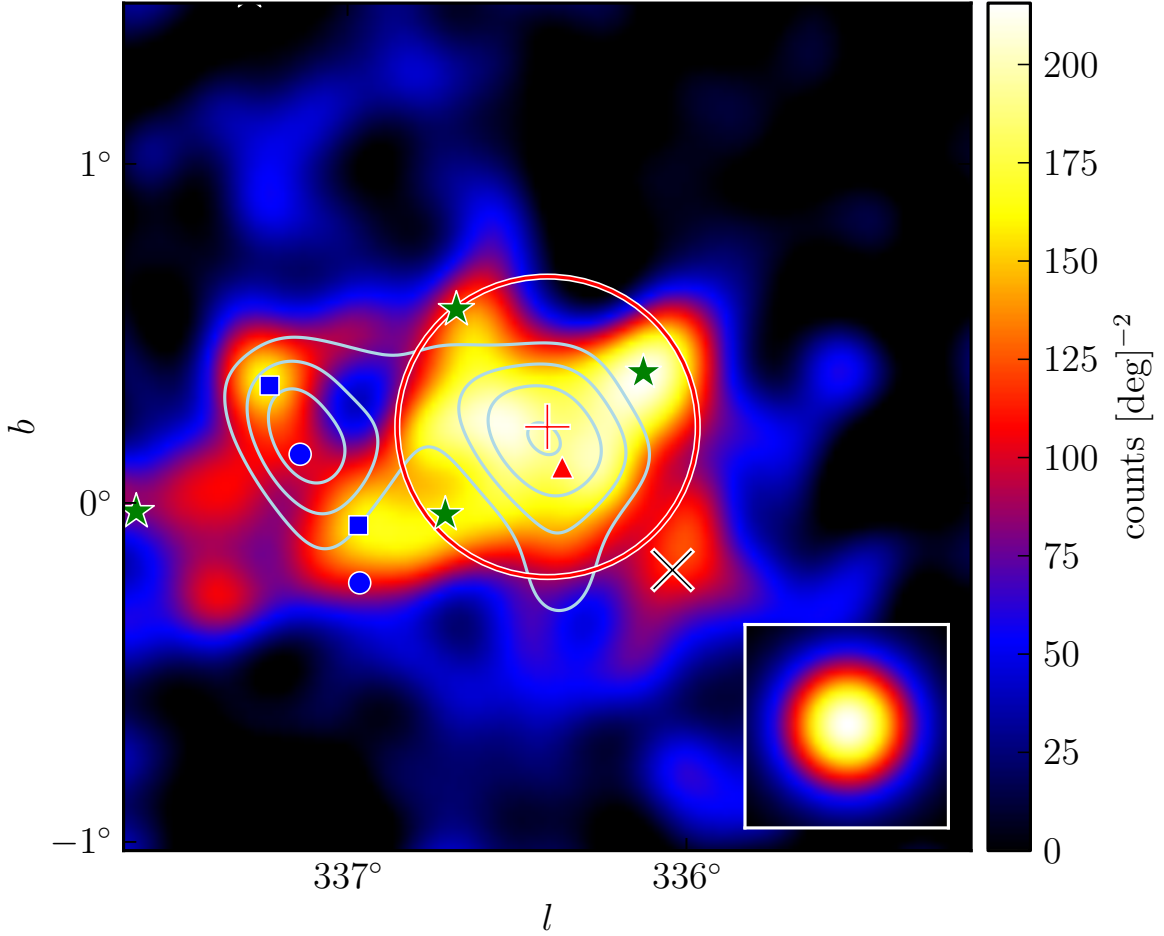


Fig. 15.— A diffuse-emission-subtracted 10 GeV to 100 GeV counts map of the region around 2FGL J1632.4–4753c smoothed by a 0.1° 2D Gaussian kernel. The triangular marker (colored red in the electronic version) represents the 2FGL position of this source. The plus-shaped marker and the circle (colored red) are the best fit position and extension 2FGL J1632.4–4753c assuming a radially symmetric uniform surface brightness. The four star-shaped markers (colored red) represent 2FGL sources that were removed from the background model. The circular and square markers (colored blue) represent the 2FGL and relocalized positions respectively of (from left to right) 2FGL J1635.4–4717c and 2FGL J1636.3–4740c. The contours (colored light blue) correspond to the TeV image of HESS J1632-478 (Aharonian et al. 2006).

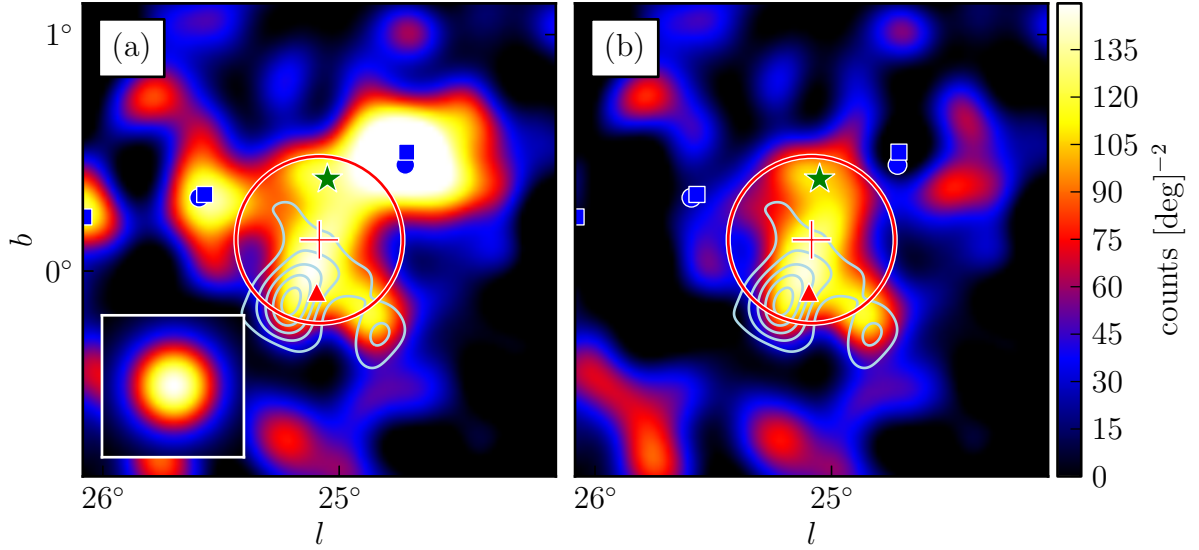


Fig. 16.— A diffuse-emission-subtracted 10 GeV to 100 GeV counts map of the region around 2FGL J1837.3–0700c (a) smoothed by a 0.1° 2D Gaussian kernel and (b) with the emission from the background sources subtracted. The triangular marker (colored red in the online version) represents the 2FGL position of this source. The plus-shaped marker and the circle (colored red) represent the best fit position and extension of 2FGL J1837.3–0700c assuming a radially symmetric uniform surface brightness. The circular and square markers (colored blue) represent the 2FGL and the relocalized position of (from left to right) 2FGL J1839.3–0558c, 2FGL J1836.8–0623c, and 2FGL J1834.7–0705c. The star-shaped marker (colored green) represent a 2FGL source that was removed from the background model. The contours (colored light blue) correspond to the TeV image of HESS J1837–069 (Aharonian et al. 2006).

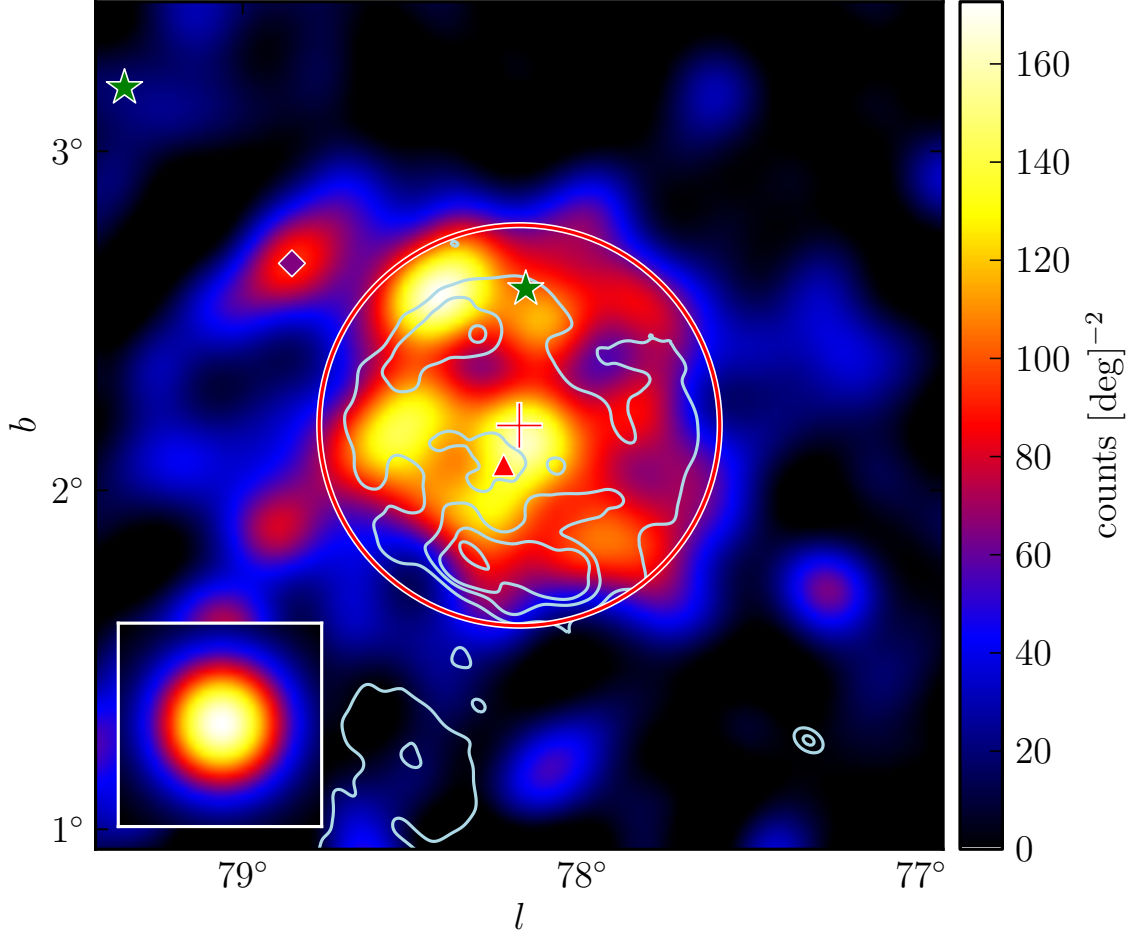


Fig. 17.— A Diffuse-emission-subtracted subtracted 10 GeV to 100 GeV counts map of the region around 2FGL J2021.5+4026 smoothed by a 0.1° 2D Gaussian kernel. The triangular marker (colored red in the online version) represents the 2FGL position of this source. The plus-shaped marker and the circle (colored red) represent the best fit position and extension of 2FGL J2021.5+4026 assuming a radially symmetric uniform surface brightness. The star-shaped markers (colored green) represent 2FGL sources that were removed from the background model. The diamond-shaped marker (colored purple) represents the position of a source not in 2FGL that was added to the region. 2FGL J2021.5+4026 is spatially coincident with the γ -Cygni SNR. The contours (colored light blue) correspond to the 408MHz image of γ -Cygni observed by the Canadian Galactic Plane Survey.

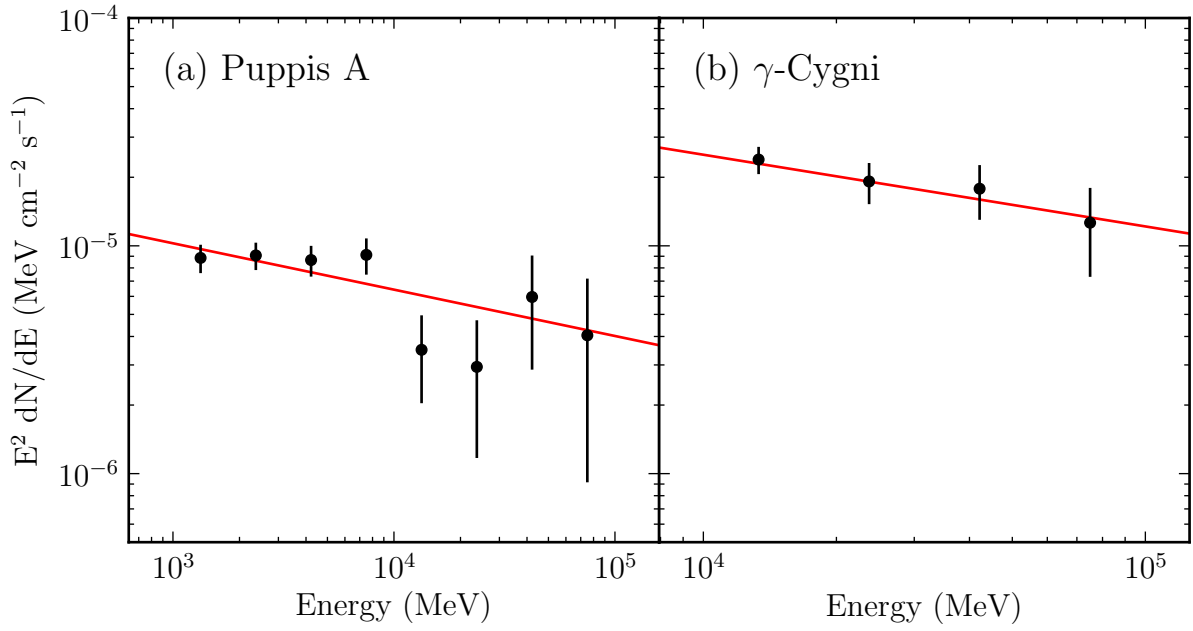


Fig. 18.— The spectral energy distribution of the extended sources Puppis A (2FGL J0823.0–4246) and γ -Cygni (2FGL J2021.5+4026). The lines (colored red in the online version) are the best fit power-law spectral model of these sources. The spectral errors are statistical only.

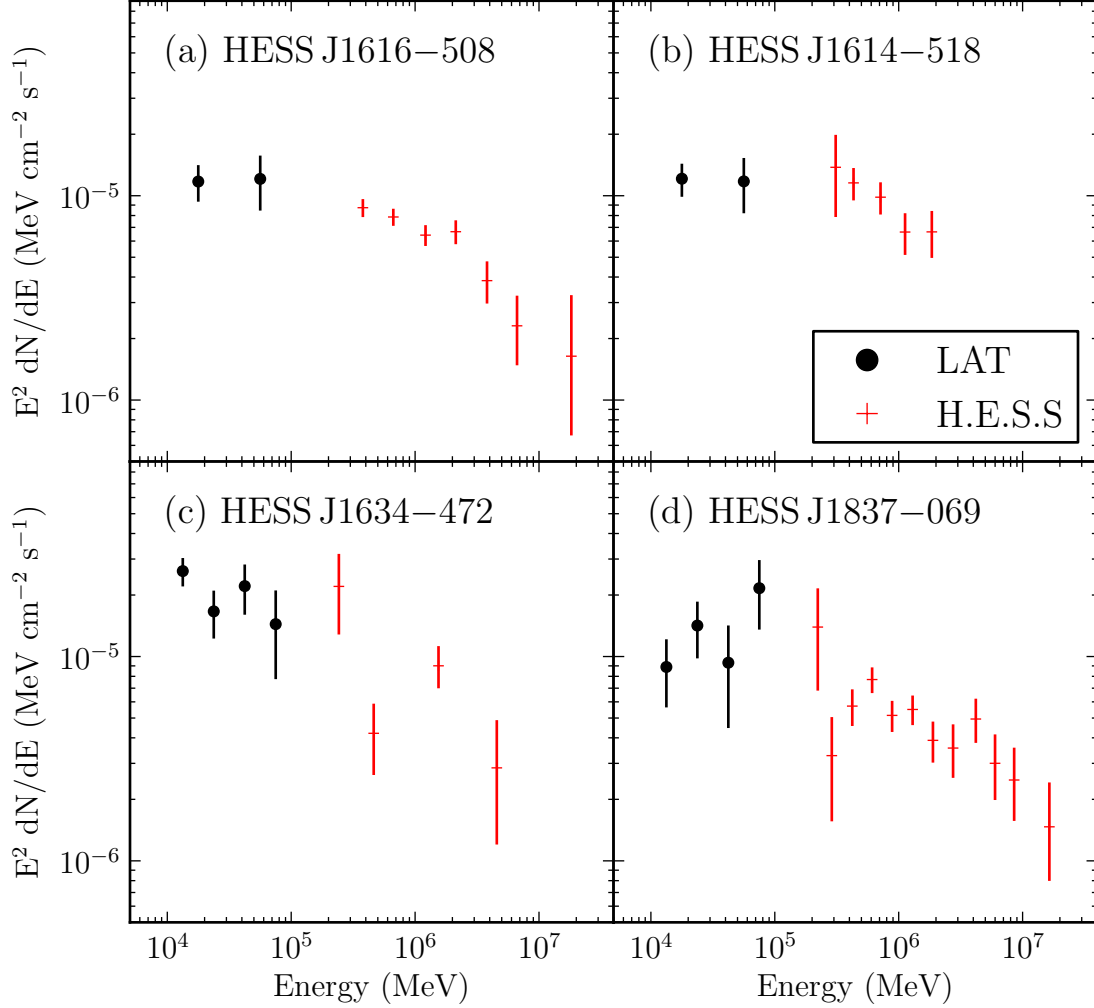


Fig. 19.— The spectral energy distribution of four extended sources associated with unidentified extended TeV sources. The black points with circular markers are the LAT data points. The points with dashed markers (colored red in the electronic version) are the H.E.S.S. points of the associated sources. Plot (a) shows the LAT SED of 2FGL J1615.0–5051 together with the H.E.S.S. SED of HESS J1616–508. Plot (b) shows 2FGL J1615.2–5138 and HESS J1614–518. Plot (c) shows 2FGL J1632.4–4753c and HESS J1632–478. Plot (d) shows 2FGL J1837.3–0700c and HESS J1837–069. The H.E.S.S. data points are from (Aharonian et al. 2006) Both LAT and H.E.S.S. spectral errors are statistical only.

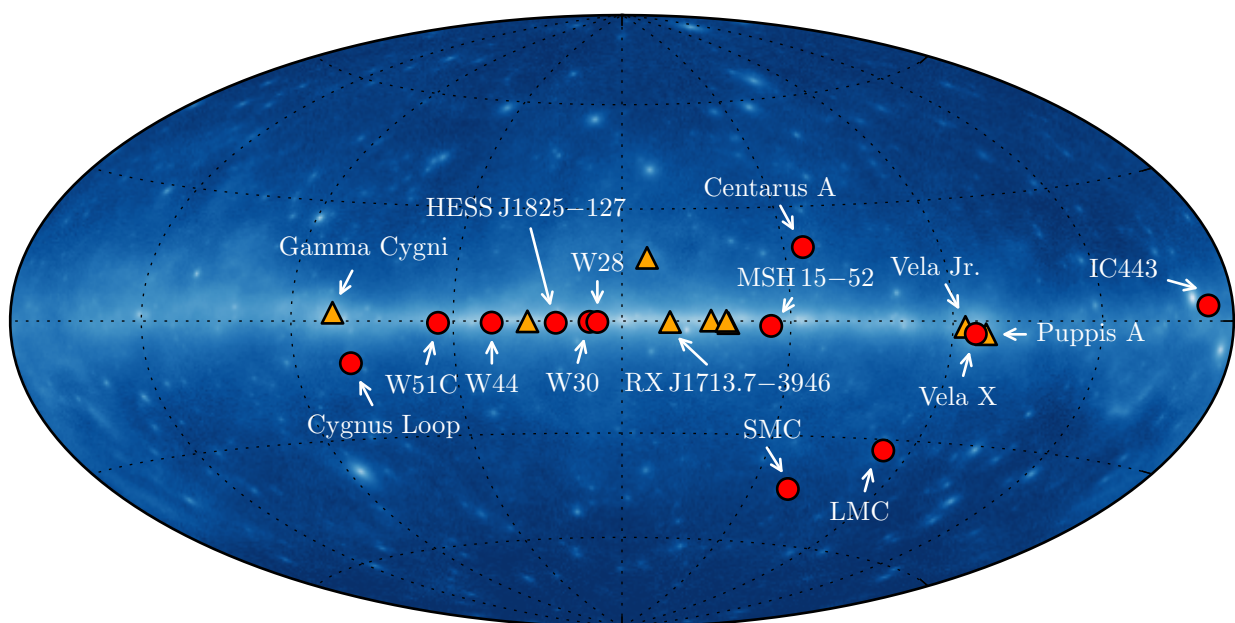


Fig. 20.— A plot of the 21 spatially extended sources detected by the LAT in the GeV energy range with two years of data. The twelve extended sources included in 2FGL are represented by the circular markers (colored red in the online version). The nine new extended sources are represented by the triangular markers (colored orange).

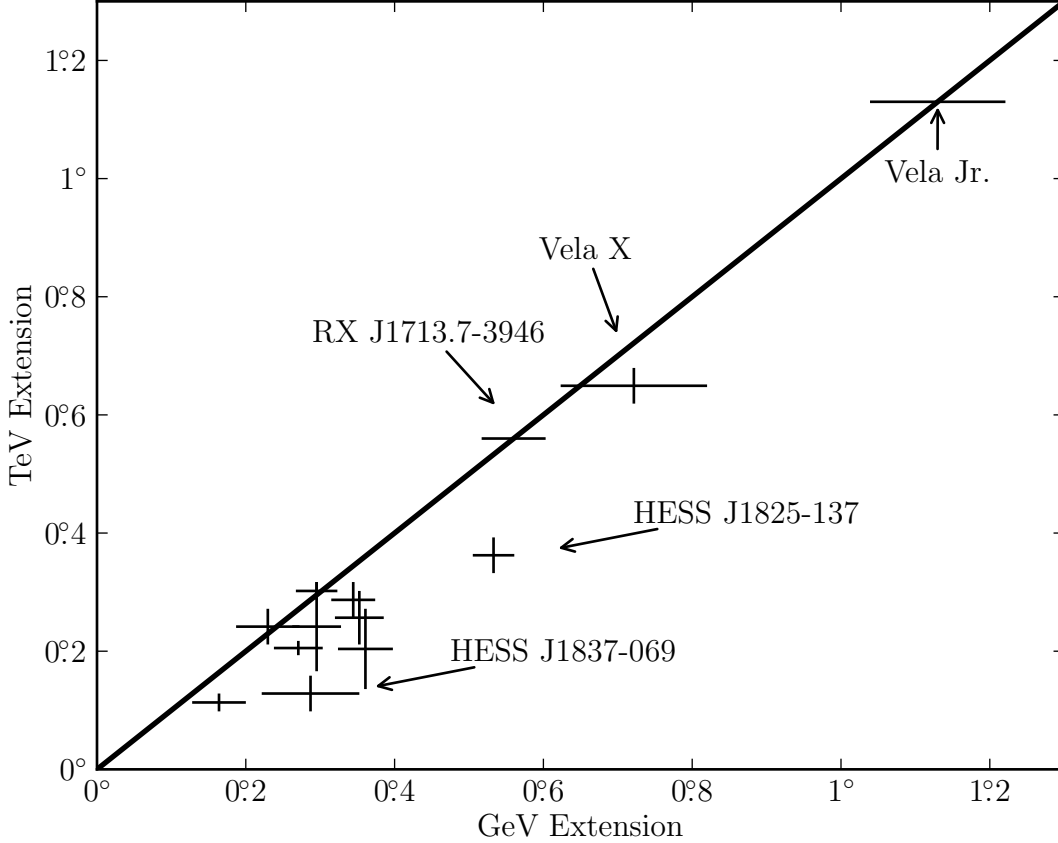


Fig. 21.— A comparison of the size of extended sources detected at both GeV and TeV energies. The TeV extensions of W30, 2FGL J1837.3–0700c, 2FGL J1632.4–4753c, 2FGL J1615.0–5051, and 2FGL J1615.2–5138 are from Aharonian et al. (2006). The TeV extensions of MSH 15–52, HESS J1825–137, Vela X, Vela Jr., RX J1713.7–3946 and W28 are from Aharonian et al. (2005, 2006b,c, 2007a,b, 2008). The TeV extension of IC443 is from Acciari et al. (2009) and W51c is from Krause et al. (2011). The TeV size of MSH 15–52, HESS J1614–518, HESS J1632–478, and HESS J1837–069 have only been reported with an elliptical 2D Gaussian fit and so the assumed size is the average of the semi-major and semi-minor axis. The LAT extension of Vela X is from Abdo et al. (2010f). Except for RX J1713.7–3946 Vela Jr., the TeV sources were fit assuming a 2D Gaussian surface brightness so the plotted GeV and TeV extensions were first converted to r_{68} (see Section 2.5). Because of their large size, the shape of RX J1713.7–3946 and Vela Jr. were not directly fit in TeV energies. Here, we take their sizes to be the same as the LAT size and do not converted them to r_{68} . The LAT extension errors are the statistical and systematic errors added in quadrature.

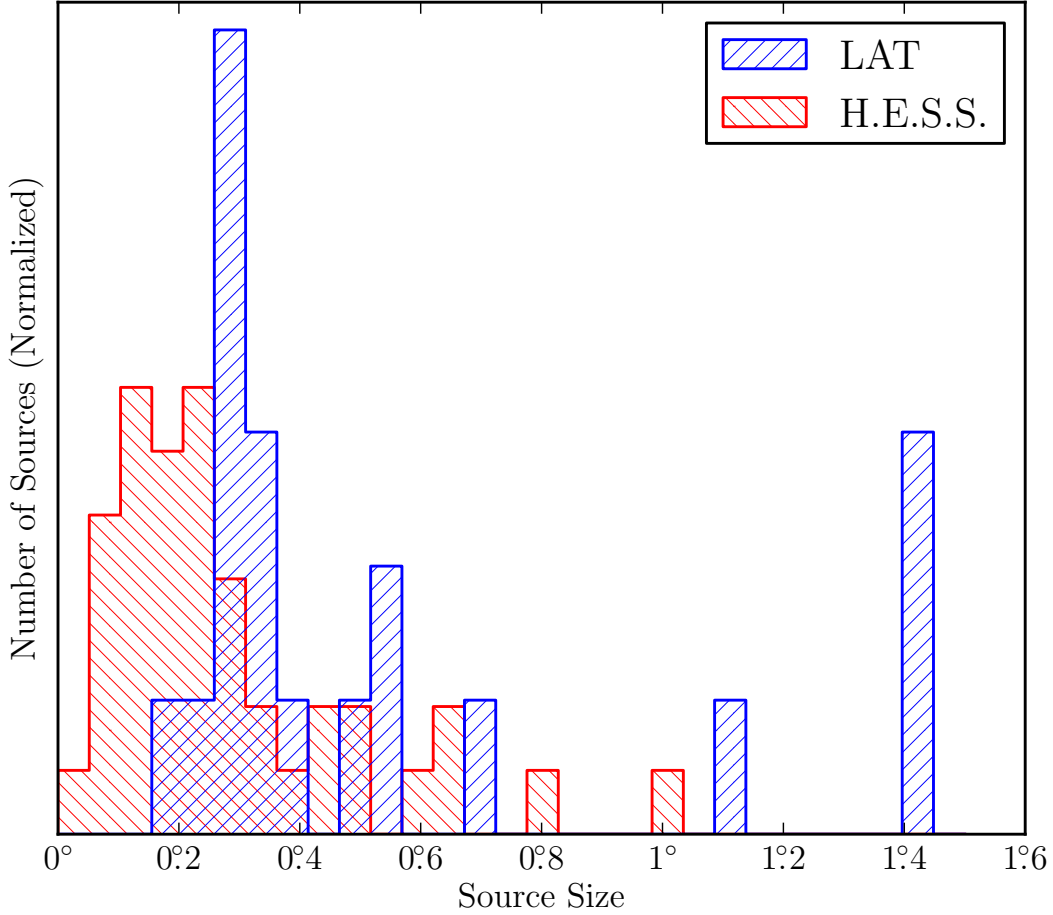


Fig. 22.— The distribution of the size of the 22 extended LAT sources at GeV energies (colored blue in the electronic version) and the size of the 42 extended H.E.S.S. sources at TeV energies (colored red). The size of Vela X is taken from Abdo et al. (2010f). Except for RX J1713.7–3946 and Vela Jr., the H.E.S.S. sources were fit with a 2D Gaussian surface brightness model so the LAT and H.E.S.S. sizes are first converted to r_{68} . (see Section 2.5). Because the spatial morphology of RX J1713.7–3946 and Vela Jr. is poorly matched by a 2D Gaussian surface brightness model, the GeV and TeV extensions are included assuming a uniform surface brightness.

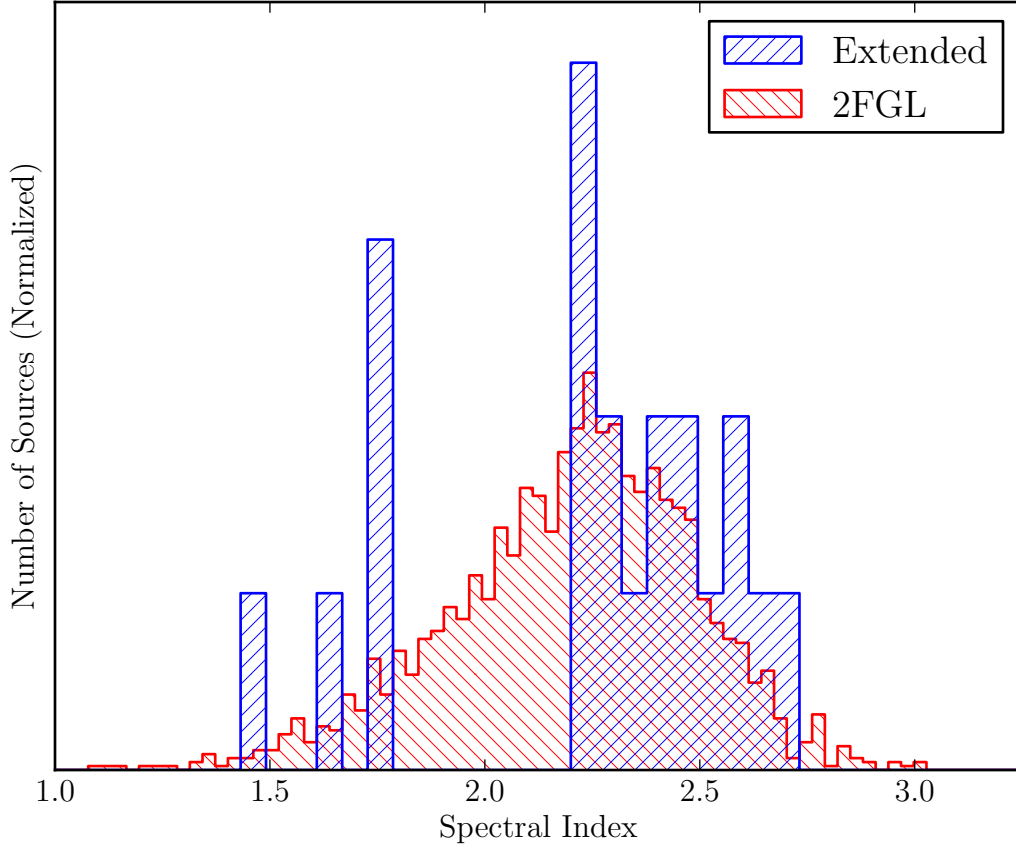


Fig. 23.— The distribution of spectral indices of the 1873 2FGL sources (colored red in the electronic version) and the 21 spatially extended sources (colored blue). The index of Centarus A is taken from Abdo et al. (2011b) and the index of Vela X is taken from Abdo et al. (2010f).